РОССИЙСКИЙ ГОСУДАРСТВЕННЫЙ ПЕДАГОГИЧЕСКИЙ УНИВЕРСИТЕТ им. А. И. ГЕРЦЕНА
HERZEN STATE PEDAGOGICAL UNIVERSITY of RUSSIA

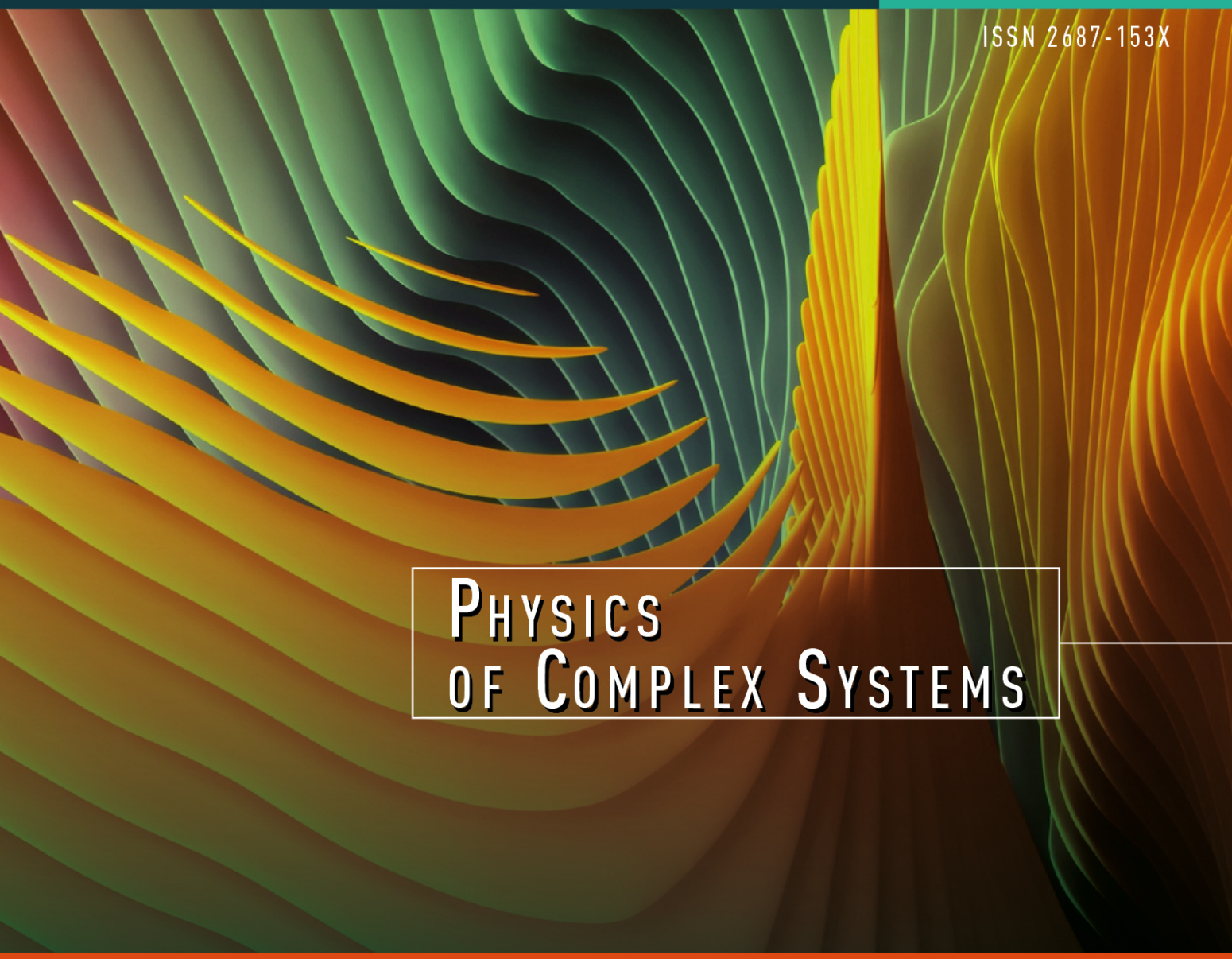

ISSN 2687-153X

Physics of Complex Systems

Т. 2 № 2 2021

Vol. 2 No. 2 2021

Herzen State Pedagogical University of Russia

ISSN 2687-153X (online)
physcomsys.ru
https://www.doi.org/10.33910/2687-153X-2021-2-2
2021. Vol. 2, no. 2

PHYSICS OF COMPLEX SYSTEMS

Mass Media Registration Certificate El No. FS77-77889, issued by Roskomnadzor on 10 February 2020
Peer-reviewed journal
Open Access
Published since 2020
4 issues per year

Publishing house of Herzen State Pedagogical University of Russia
48 Moyka Emb., St Petersburg 191186, Russia
E-mail: izdat@herzen.spb.ru
Phone: +7 (812) 312-17-41

Data size 4,99 Mbyte
Published at 29.05.2021

Editors of the English text *I. A. Nagovitsyna, A. S. Samarsky*
Cover design by *O. V. Rudneva*
Layout by *A. M. Khodan, L. N. Kliuchanskaya*

CONTENTS

Condensed Matter Physics. Physics of Low-Dimensional Structures and Nanostructures

UDC 548.4

https://www.doi.org/10.33910/2687-153X-2021-2-2-51-60

A model of strain hardening in nanoceramics with amorphous intercrystalline layers

M. Yu. Gutkin✉[1], K. N. Mikaelyan[1]

[1] Institute for Problems in Mechanical Engineering of the Russian Academy of Sciences,
61 Bolshoy Ave., Saint Petersburg 199178, Russia

Authors

Mikhail Yu. Gutkin, ORCID: 0000-0003-0727-6352, e-mail: m.y.gutkin@gmail.com

Kristina N. Mikaelyan, e-mail: kristy_mik@gmail.com

For citation: Gutkin, M. Yu., Mikaelyan, K. N. (2021) A model of strain hardening in nanoceramics with amorphous intercrystalline layers. *Physics of Complex Systems*, 2 (2), 51–60. https://www.doi.org/10.33910/2687-153X-2021-2-2-51-60

Received 17 March 2021; reviewed 30 March 2021; accepted 30 March 2021.

Abstract. The article suggests a theoretical model which describes the development of plastic deformation within amorphous intercrystalline layers in nanocrystalline ceramics as a process of homogeneous generation of inclusions of the liquid-like phase, their extension and further penetration to neighbouring layers through triple junctions. The energetic characteristics of these stages are calculated and analysed in detail. It is shown that the nucleation stage can be realised in the barrier-less regime when the applied shear stress reaches its critical value which depends on the temperature of the mechanical testing. The penetration stage of the deformation process needs some increase in the applied shear stress and, therefore, leads to strain hardening of the model nanocrystalline ceramics. The corresponding flow stress increases with diminishing grain size of the nanoceramics and lowering temperature of testing.

Keywords: nanocrystalline ceramics, amorphous intercrystalline layers, inclusions, liquid-like phase, plastic deformation, strain hardening.

Introduction

It is well known that in certain ceramics with covalent chemical bonding like Al_2O_3, SiC, Si_3N_4, $SrTiO_3$, etc., the grain boundaries (GBs) can contain amorphous films of about 1–2 nm thickness, which are also called 'intergranular glassy films' (IGFs). Earlier research by D. R. Clarke was aimed at the detection of IGFs with electron microscopy (Clarke 1979) and explanation of their existence and stability (Clarke 1987). Many experimental observations were made by Rühle's group (see, for example, Kleebe et al. 1992; 1993). These and other related results on IGFs in ceramics and ceramic matrix composites are presented in collective monographs (Dufour et al. 1989; Hoffmann, Petzow 1994; Tomsia, Glaeser 1998) and reviews (Kleebe 1997; Subramaniam et al. 2006). In particular, it was shown that IGFs have a nearly constant thickness which is basically independent of the orientation of the bounding grains, but is dependent on the composition of ceramics (Subramaniam et al. 2006). The presence of IGFs can play an important role in determining the properties of ceramics as a whole, such as strength, toughness, fatigue, etc. (Hoffmann, Petzow 1994; Chen et al. 2000). It is worth noting that IGFs in ceramic silicon nitride attract special attention of many researchers (Clarke 1979; 1987; Hoffmann, Petzow 1994; Kleebe et al. 1992; 1993; Zhang et al. 2011).

Extensive investigations in the field of nanocrystalline materials have stimulated the interest in IGFs in nanocrystalline ceramics (Keblinski et al. 1996; 1997; Mo, Szlufarska 2007; Szlufarska et al. 2005) in relation to their outstanding mechanical properties (Hulbert et al. 2007; Xu et al. 2006). Since the experimental observations in this field are extremely complicated and laborious, a significant role

is played by computer simulations (Demkowicz et al. 2007; Demkowicz, Argon 2004; 2005a; 2005b; Keblinski et al. 1996; 1997; Mo, Szlufarska 2007; Szlufarska et al. 2005) and analytical theoretical models (Bobylev et al. 2008; Bobylev, Ovid'ko 2008; Glezer, Pozdnyakov 1995; Gutkin, Ovid'ko 2009; 2010a; 2010b; Ovid'ko et al. 2008; Pozdnyakov, Glezer 1995). Thus, computer simulation results give a basis for developing theoretical analytical models which, in their turn, show directions for further computer simulations.

In particular, researchers (Demkowicz, Argon 2004; 2005a; 2005b) simulated bulk amorphous silicon (a-Si) as a typical amorphous covalent material and showed that its atomic structure includes liquid-like and solid-like regions. The volume fractions of these components depend on the cooling rate of liquid silicon, which leads to a change in the plastic flow regime of the simulated samples—the higher the volume fraction of the liquid-like material is, the more homogeneous the plastic flow of a-Si is. Moreover, the fraction of the liquid-like phase increases under mechanical loading. The authors concluded that the liquid-like phase regions are the carriers of plastic deformation in a-Si. Since the latter is a typical example of an amorphous covalent material, they suggested that these features are also inherent in other amorphous solids with covalent bonding, in particular, in GB layers of amorphous silicon nitride (a-Si_3N_4) surrounding the titanium nitride nanograins (nc-TiN) in nc-TiN/a-Si_3N_4 ceramic nanocomposite. Later, the formation and growth of the liquid-like phase regions in the GBs were observed in a computer simulation of the plastic deformation of nc-Si (Demkowicz et al. 2007).

Based on the results of the computer simulations (Demkowicz, Argon 2004; 2005a; 2005b; Demkowicz et al. 2007), a theoretical model of the plastic deformation of an amorphous covalent material was suggested in (Gutkin, Ovid'ko 2009; 2010a) and later used for the description of the mechanical behaviour of amorphous intercrystalline layers in nanoceramics (Gutkin, Ovid'ko 2009; 2010b). This model describes the following main features of the plastic deformation of amorphous covalent material (Gutkin, Ovid'ko 2010a):

(1) The mechanism of plastic deformation is the homogeneous nucleation and development of liquid-like phase inclusions under the applied shear stress.
(2) Such inclusions exhibit a plastic shear modelled by glide dislocation loops, which appear and develop simultaneously with the inclusions.
(3) The formation of such inclusions does not require overcoming the energy barrier if the applied stress reaches some critical temperature-dependent level; the higher the temperature is, the lower the critical stress is.
(4) In the case of the barrierless nucleation of the inclusion at relatively low temperatures, the strength (the Burgers vector) of the dislocation loop, which models the plastic shear inside the inclusion, increases faster than the loop size. In this case, the heterogeneous plastic flow of the amorphous material due to the concentration of the plastic deformation in narrow slip bands should be expected.
(5) If the barrierless nucleation of the inclusion proceeds at a relatively high temperature, an increase in the size of the dislocation loop advances an increase in its strength and a homogeneous plastic flow of the material via the bulk nucleation and gradual development of such inclusions should be expected. If, in addition, the applied stress exceeds the critical level for the barrierless nucleation of inclusions, the transition from the homogeneous to heterogeneous flow of the amorphous material becomes possible.

For a model case of nc-TiN/a-Si_3N_4 ceramic nanocomposite, the papers (Gutkin, Ovid'ko 2009; 2010b) show that, when the length of the amorphous layer is large enough and a considerable dislocation charge is accumulated, the inclusions of the liquid-like phase induce the formation and growth of mode I–II cracks in neighbouring amorphous layers. In this case, the possibility of opening and growing the crack depends very strongly on the test temperature, the layer orientation, and the size of nanoceramic grains. An increase in the temperature and the angle of orientation and a decrease in the size of nanoceramic grains favour an increase in the crack resistance.

In the present paper, we consider another scenario of the plastic deformation development when the crack opening is suppressed. In this case, it is assumed that the inclusion of the liquid-like phase can overcome the triple junction of amorphous intercrystalline layers and penetrate into one of the neighbouring layers. We show that this process needs some increase in the applied shear stress and, therefore, leads to strain hardening of model nanocrystalline ceramics.

 https://www.doi.org/10.33910/2687-153X-2021-2-2-51-60

Model

According to the approach proposed in (Gutkin, Ovid'ko 2009; 2010a), we consider a model nanoceramic sample, to which a normal tensile stress σ is applied, and one of the amorphous intergranular interlayers of length L and thickness h, in which the maximum shear stress $\tau = \sigma / 2$ acts (Fig. 1). Based on the results (Gutkin, Ovid'ko 2009; 2010a), we assume that until this stress reaches a certain critical value $\tau = \tau_c$, the sample is elastically deformed. Upon reaching the critical stress τ_c, which corresponds to the critical elastic shear deformation $\varepsilon_c = \tau_c /(2G)$, where G is the shear modulus, a nucleus of a liquid-like phase with plastic shear localised in it is formed in the amorphous interlayer without any energy barrier. For the sake of simplicity, the local plastic shear is modelled here by a dipole of edge dislocations with variable Burgers vectors $\pm s$. Under the action of stress $\tau \geq \tau_c$, the longitudinal size p of the nucleus grows and reaches the length of the amorphous interlayer L. At the same time, the magnitude s of the Burgers vector also increases. As shown by the calculations (Gutkin, Ovid'ko 2009; 2010a), the value of s in the first approximation is directly proportional to the size of the nucleus p: $s \approx \eta\rho$, $\eta<1$. At relatively low temperatures of the deformation test, the calculations (Gutkin, Ovid'ko 2009; 2010a) show $\eta \approx 0.2$, while at relatively high temperatures they show $\eta \approx 0.05$.

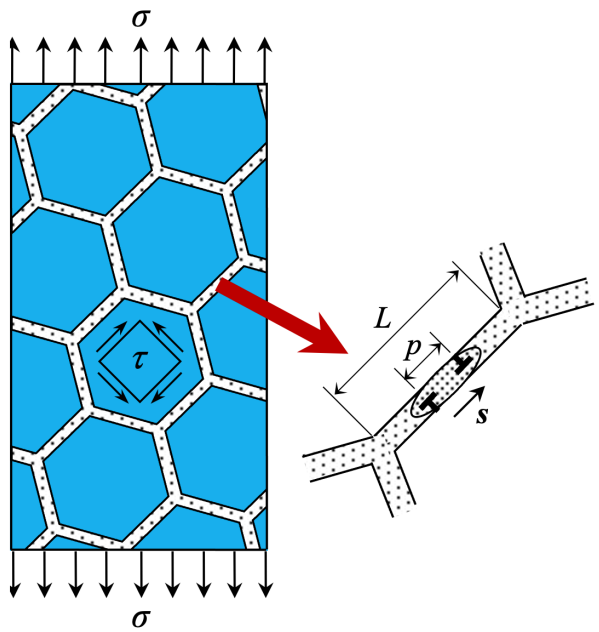

Fig. 1. A two-dimensional model of the plastic flow of nanoceramics due to the formation of nuclei of the liquid-like phase in the grain boundaries in which plastic shear develops, simulated by a dipole of edge dislocations with a growing Burgers vector **s**

Let us use this model to calculate stress-strain curves for such a model nanoceramic sample. The plastic deformation of the sample can be estimated with the following formula (Ovid'ko, Sheinerman 2009):

$$\varepsilon \approx \alpha \frac{s}{d} \approx \alpha\eta \frac{p}{d}, \tag{1}$$

where α is the fraction of grain boundaries oriented in such a way that a given stress τ acts in them (Ovid'ko, Sheinerman 2009), and d is the average grain size of the sample.

The formation and growth of one nucleus of a liquid-like phase in a grain boundary with a suitable orientation in nanoceramics is accompanied by a change in the energy of the system (per unit dislocation length) by the value

$$\Delta W = W_d + HS - \tau s p, \tag{2}$$

where W_d is the strain energy of the dislocation dipole, H is the excess enthalpy of the liquid-like phase in comparison with the solid-like phase, and S is the cross-sectional area of the nucleus of the liquid-like

phase. Assuming that the arm of the dipole is approximately equal to the longitudinal size of the nucleus p, we can write the strain energy W_d as follows (Gutkin, Ovid'ko, Skiba 2004):

$$W_d = \frac{Gs^2}{2\pi(1-\nu)} \ln \frac{p-r_c}{r_c} \approx \frac{G\eta^2 p^2}{2\pi(1-\nu)} \ln \frac{1-\eta}{\eta}, \quad (3)$$

where ν is the Poisson ratio, $rc \approx s \approx \eta\rho$ is the cutoff radius of the elastic field of the dipole at the dislocation lines. For simplicity, we will assume that $S = pt \approx p\xi b$, where t is the transverse size of the nucleus, $\xi \approx 2...4$, and b is the average interatomic distance.

With Eq. (3) and the assumptions made, Eq. (2) takes the following form:

$$\Delta W = \frac{G\eta^2 p^2}{2\pi(1-\nu)} \ln \frac{1-\eta}{\eta} + H\xi bp - \tau\eta p^2. \quad (4)$$

Results

In the numerical investigation of the energy change ΔW, we used the material characteristics for nanoceramic silicon nitride (Si_3N_4) as was the case in (Gutkin, Ovid'ko 2009; 2010b): $G = 120$ GPa, $\nu = 0.2$, and $b \approx 0.174$ nm; at relatively low temperatures of testing, we took $H = 0.05$ eV/at. and $n \approx 0.2$, while at relatively high temperatures of testing, $H = 0.01$ eV/at. and $n \approx 0.05$. For the sake of definiteness, it was also assumed that $\xi \approx 2$.

Fig. 2 shows the dependences $\Delta W(p)$ plotted at different values of the applied shear stress τ for relatively (a) low and (b) high temperatures. It is seen that, depending on the level of τ, the curves $\Delta W(p)$ can demonstrate rather different behaviours. They can monotonously increase at relatively low values of τ, or first increase, reach their maxima and then decrease at some intermediate values of τ, or monotonously decrease at relatively high values of τ. In the first case, the formation of the liquid-like phase nucleus is energetically unfavourable and, therefore, impossible. In the second and third cases, the nucleus formation is possible if the corresponding energy barrier is either small enough or even absent.

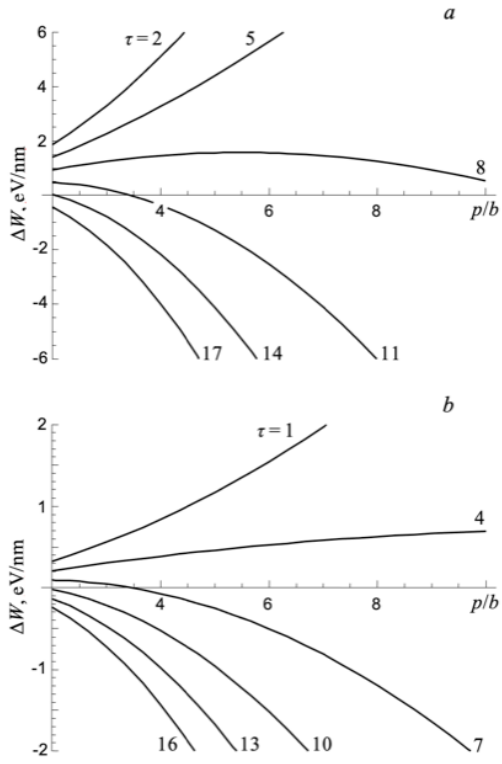

Fig. 2. Dependence of the energy change ΔW on the normalised size p/b of the nucleus of the liquid-like phase for different values of the applied shear stress τ (in units of GPa) at (a) low and (b) high temperatures

 https://www.doi.org/10.33910/2687-153X-2021-2-2-51-60

The most strict and reliable conditions for the nucleus formation event are that (i) the energy change ΔW is not positive for some initial nucleus size, and (ii) the energy change ΔW monotonously decreases with the nucleus size p. It is seen from the plots shown in Fig. 2 that these conditions are satisfied if τ eaches a critical value, $\tau = \tau_c(T)$. At relatively low temperatures, $\tau_c \approx 14$ *GPa*, while at relatively high temperatures, $\tau_c \approx 9.5$ *GPa*.

It also follows from these plots that at stress values equal to or higher than the critical one, the nucleus of the liquid-like phase develops in an unstable regime. Obviously, this happens until it reaches the nearest obstacle, which, in the case of nanoceramics, is the nearest triple junction of grain boundaries. Overcoming the triple junction leads to a displacement of the boundary that is not subjected to the shear (Fig. 3) and to the formation (in the case of tilt boundaries) of a dipole of partial wedge disclinations of strength ω equal to the misorientation angle of this boundary and with an arm equal to the displacement of the boundary (Ovid'ko, Sheinerman 2009). A further increase in the size of the nucleus of the liquid-like phase, accompanied by an increase in the plastic shear, causes an elongation of the disclination dipole arm and a corresponding increase in its energy, hence the appearance of a thermodynamic force that prevents the propagation of the liquid-like phase. To overcome this force, it is necessary to further increase the applied stress level. Thus, the transition of the system to the hardening stage should be expected.

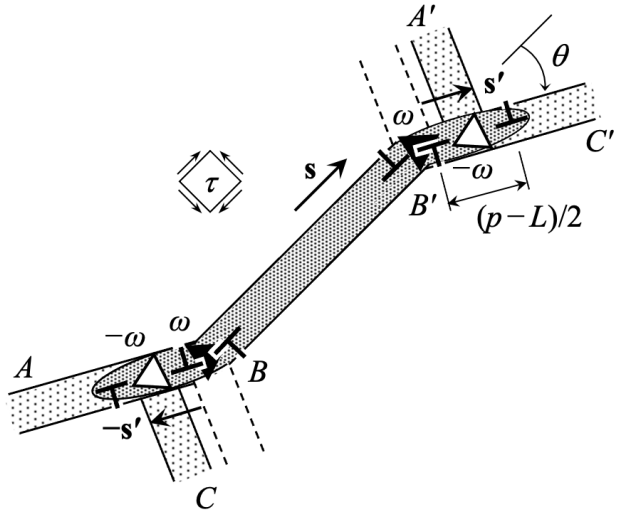

Fig. 3. Model of nucleation of the secondary nuclei of the liquid-like phase along the grain boundaries AB and B′C′. The development of the secondary nuclei of the liquid-like phase is accompanied by their plastic shear, which is modelled by two new dipoles of edge dislocations with arms $(p - L)/2$ and Burgers vectors $\pm \boldsymbol{s}'$. The plastic shears are accompanied by the displacements of the grain boundaries A′B′ and BC by vectors $\boldsymbol{s}'$ and $-\boldsymbol{s}'$, respectively, and the appearance of two dipoles of partial wedge disclinations with arms s' and strengths $\pm\omega$

To calculate the stress providing plastic deformation at the hardening stage, consider the model shown in Fig. 3. It shows the grain boundary BB′ filled with the liquid-like phase and subjected to plastic shear. This plastic shear is modelled by a dipole of edge dislocations pressed by the applied stress $\tau \geq \tau_c$ to two triple junctions B and B′, on which secondary nuclei of the liquid-like phase are generated along the neighbouring boundaries AB and B′C′. The development of these secondary nuclei of the liquid-like phase is accompanied by their plastic shear, which is modelled by two new dipoles of edge dislocations with the Burgers vector $\pm \boldsymbol{s}'$, the magnitude of which increases with an increase in the size of these nuclei $s' \approx \eta(p\text{-}L)/2$, where p is the total length of the liquid-like phase ABB′C′ and L is the length of the boundary BB′. At the same time, the boundaries BC and A′B′ are displaced in opposite directions by distances s' with the formation of two biaxial dipoles of partial wedge disclinations with arms s'. For simplicity of further calculations, we assume that the strengths of these dipoles are the same and equal to ω.

The change in the energy of the system $\Delta W'$ accompanying the formation of two secondary nuclei of the liquid-like phase (Fig. 3) can be written in the following form:

$$\Delta W' = 2W_d' + W_{qd} + W_{d,\text{int}} + H\xi\, b(p-L) - \tau\cos(2\theta)\, s'(p-L), \tag{5}$$

where $2W'_d$ is the self-strain energy of two new dislocation dipoles, W_{qd} is the self-strain energy of the disclination quadrupole, $W_{d,int}$ is the energy of the elastic interaction of the new dislocation dipoles with the old one, θ is the angle of deviation of the boundaries AB and B′C′ from the straight line BB′. Note that in the first approximation we neglect the elastic interaction of new dislocation dipoles with each other and with the 'opposite' disclination dipoles. If necessary, these terms can be taken into account, although they are unlikely to be significant.

We write the first term in Eq. (5) by analogy with Eq. (3) as follows:

$$2W_d = \frac{2Gs'^2}{2\pi(1-\nu)} \ln \frac{(p-L)/2 - r_c}{r_c} \approx \frac{G\eta^2(p-L)^2}{4\pi(1-\nu)} \ln \frac{1-\eta}{\eta} . \tag{6}$$

The second term of Eq. (5) is approximated by the well-known expression for a disclination quadrupole in which all disclinations lie on the same line (Romanov, Vladimirov 1992). Substituting our definition of the dipole arm into this expression, after some algebra we have

$$W_{qd} = \frac{G\omega^2\eta^2(p-L)^2}{16\pi(1-\nu)} \left\{ \ln \frac{4L[L+\eta(p-L)]}{\eta^2(p-L)^2} + \left(\frac{2L+\eta(p-L)}{\eta(p-L)} \right)^2 \ln \frac{4L[L+\eta(p-L)]}{[2L+\eta(p-L)]^2} \right.$$
$$\left. +2 \frac{2L+\eta(p-L)}{\eta(p-L)} \ln \frac{L+\eta(p-L)}{L} \right\} . \tag{7}$$

The third term in Eq. (5) was calculated in (Gutkin, Ovid'ko, Pande 2004). With our denotations, it takes the following form:

$$W_{d,\text{int}} = -\frac{G\eta^2(p-L)L}{2\pi(1-\nu)} \left\{ \frac{\cos\theta}{2} \ln \frac{4L^2}{\eta^2[4L^2+4L(p-L)\cos\theta+(p-L)^2]} \right.$$
$$\left. + \frac{2L(p-L)\sin^2\theta}{4L^2+4L(p-L)\cos\theta+(p-L)^2} \right\} . \tag{8}$$

Thus, all terms of Eq. (5) are defined. Fig. 4 shows the dependence of the energy change $\Delta W'$ on the normalised size p/b of the nucleus of the liquid-like phase for L = 100b, $\omega = \pi/3$, $\theta = \pi/6$, and different values of the applied shear stress τ at (a) low and (b) high temperatures. The upper curves are plotted for the corresponding values of the critical stress τ_c = 14 and 9.5 GPa. It is seen that even at these values, it is energetically favourable for new critical nuclei to grow to significant sizes of the order of 25b ≈ 4.35 nm at low temperatures and up to 65b ≈ 11.31 nm at high temperatures. However, their further growth requires an increase in the level of τ.

In the case of quasi-static loading, we can assume (Ovid'ko, Sheinerman 2009) that each level of the stress $\tau \geq \tau_c$ will correspond to the equilibrium size of the nucleus of the liquid-like phase and, accordingly, the magnitude of plastic shear. The equilibrium condition is determined by the equation $\partial \Delta W'(p)/\partial p = 0$, from which we immediately find

$$\tau = \frac{G\eta}{4\pi(1-\nu)\cos 2\theta} \left\{ 2\ln\frac{1-\eta}{\eta} - \frac{L\cos\theta}{p-L} \ln \frac{4L^2}{\eta^2[4L^2+4L(p-L)\cos\theta+(p-L)^2]} \right.$$
$$- \frac{16L^3\sin^2\theta[2L+(p-L)\cos\theta]}{[4L^2+4L(p-L)\cos\theta+(p-L)^2]^2} + \frac{2L\cos\theta(2L\cos\theta+p-L)}{4L^2+4L(p-L)\cos\theta+(p-L)^2}$$
$$\left. +\omega^2 \left[\ln\frac{2L+2\eta(p-L)}{\eta(p-L)} + \frac{2L+\eta(p-L)}{\eta(p-L)} \ln \frac{2L+2\eta(p-L)}{2L+\eta(p-L)} \right] \right\} + \frac{H\xi b}{\eta(p-L)\cos 2\theta} . \tag{9}$$

 https://www.doi.org/10.33910/2687-153X-2021-2-2-51-60

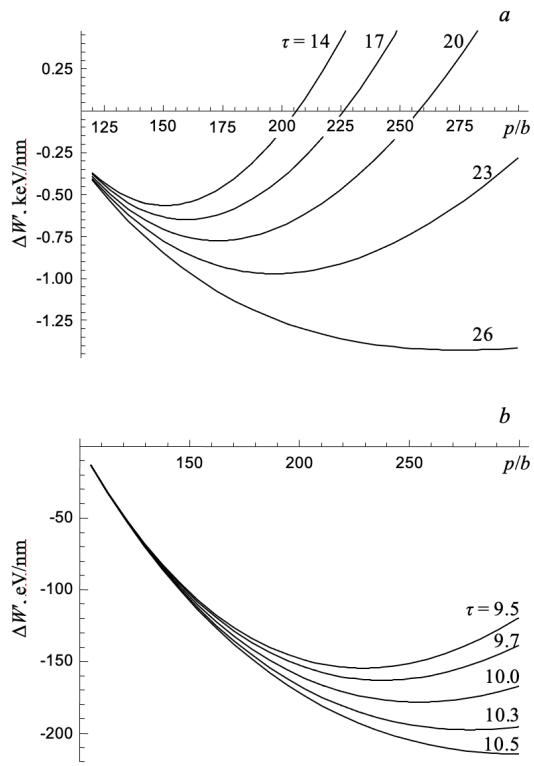

Fig. 4. Dependence of the energy change $\Delta W'$ on the normalised size p/b of the nucleus of the liquid-like phase for different values of the applied shear stress τ (in units of GPa) at (a) low and (b) high temperatures.

Let us now find the plastic deformation occurring in the plane of the grain boundary BB′. It can be estimated by the sum

$$\varepsilon = \varepsilon_1 + \varepsilon_2 , \tag{10}$$

where ε_1 is the plastic deformation due to the shear inside the primary nucleus of the liquid-like phase, which is determined by formula (1) at $p = L$:

$$\varepsilon_1 \approx \alpha\eta \frac{L}{d} , \tag{11}$$

and ε_2 is the plastic deformation due to the shear inside the secondary nuclei of the liquid-like phase, which, by analogy, can be written as

$$\varepsilon_2 \approx \alpha\eta \frac{(p-L)\cos\theta}{2d} . \tag{12}$$

Then it follows from Eq. (10) with Eqs. (11) and (12) that

$$p - L \approx \frac{2}{\cos\theta}\left(\frac{\varepsilon d}{\alpha\eta} - L\right). \tag{13}$$

Now, assuming that $d \approx 1.5L$, we can make the substitution $p - L \approx L[3\varepsilon/(\alpha\eta)-2]/\cos\theta$ in Eq. (9), which gives the dependence $\tau(\varepsilon)$.

Fig. 5 shows the curves $\tau(\varepsilon)$ plotted for different values of the grain boundary length L at relatively (a) low and (b) high temperatures. It is seen that grain refinement (shortening of grain boundaries) of nanoceramics leads to some increase in the flow stress.

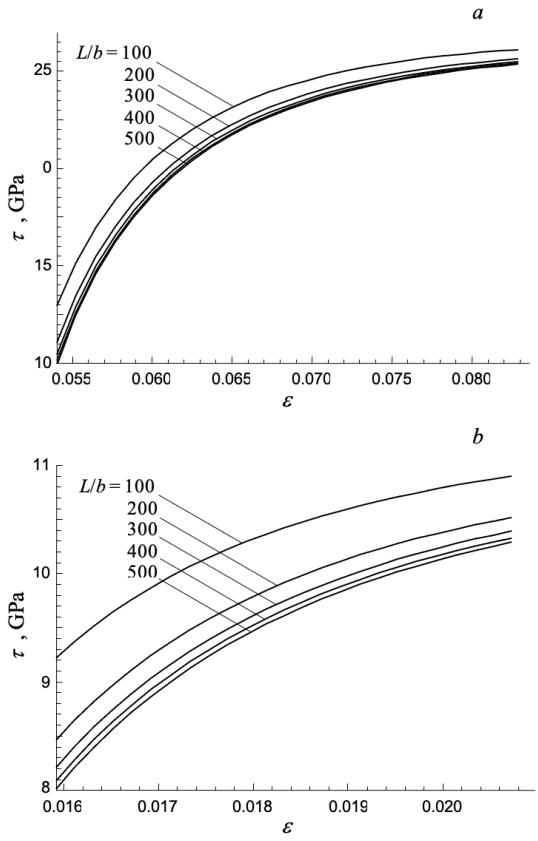

Fig. 5. Dependence of the shear stress on the plastic deformation at the stage of hardening of Si_3N_4 nanoceramics for different lengths L of the grain boundaries at relatively (a) low and (b) high temperatures

Thus, we have considered the case of penetration of an inclusion of the liquid-like phase from one amorphous intercrystalline layer to another through a triple junction of such layers, which is alternative to the case of the crack opening at the triple junction studied in (Gutkin, Ovid'ko 2009; 2010b). We have shown that this process needs some increase in the applied shear stress and, therefore, leads to strain hardening of the model nanoceramics. The corresponding flow stress increases with diminishing grain size of the nanoceramics and is higher for low temperatures than for high temperatures.

Conclusion

In summary, the study suggests a theoretical model which describes the development of plastic deformation within amorphous intercrystalline layers in nanocrystalline ceramics as a process of homogeneous generation of inclusions of the liquid-like phase, their extension and further penetration to neighbouring layers through their triple junctions. The energetic characteristics of these stages are calculated and analysed in detail.

It is shown that the nucleation stage can be realised in the barrier-less regime when the applied shear stress reaches its critical value which depends on the temperature of the mechanical testing. The higher the temperature is, the smaller the critical stress is.

The penetration stage of the deformation process needs some increase in the applied shear stress and, therefore, leads to strain hardening of model nanocrystalline ceramics. The corresponding flow stress increases with diminishing grain size of nanoceramics. The higher the temperature is, the smaller the flow stress is.

References

Bobylev, S. V., Gutkin, M. Yu., Ovid'ko, I. A. (2008) Plastic deformation transfer through the amorphous intercrystallite phase in nanoceramics. *Physics of the Solid State*, 50 (10), 1888–1894. https://doi.org/10.1134/S106378340810017X (In English)

Bobylev, S. V., Ovid'ko, I. A. (2008) Dislocation nucleation at amorphous intergrain boundaries in deformed nanoceramics. *Physics of the Solid State*, 50 (4), 642–648. https://doi.org/10.1134/S1063783408040082 (In English)

Chen, D., Zhang, X.-F., Ritchie, R. O. (2000) Effects of grain-boundary structure on the strength, toughness, and cyclic-fatigue properties of a monolithic silicon carbide. *Journal of the American Ceramic Society*, 83 (8), 2079–2081. https://doi.org/10.1111/j.1151-2916.2000.tb01515.x (In English)

Clarke, D. R. (1979) On the detection of thin intergranular films by electron microscopy. *Ultramicroscopy*, 4 (1), 33–44. https://doi.org/10.1016/0304-3991(79)90006-8 (In English)

Clarke, D. R. (1987) On the equilibrium thickness of intergranular glass phases in ceramic materials. *Journal of the American Ceramic Society*, 70 (1), 15–22. https://doi.org/10.1111/j.1151-2916.1987.tb04846.x (In English)

Demkowicz, M. J., Argon, A. S. (2004) High-density liquidlike component facilitates plastic flow in a model amorphous silicon system. *Physical Review Letters*, 93 (2), article 025505. https://doi.org/10.1103/PhysRevLett.93.025505 (In English)

Demkowicz, M. J., Argon, A. S. (2005a) Autocatalytic avalanches of unit inelastic shearing events are the mechanism of plastic deformation in amorphous silicon. *Physical Review B*, 72 (24), article 245206. https://doi.org/10.1103/PhysRevB.72.245206 (In English)

Demkowicz, M. J., Argon, A. S. (2005b) Liquidlike atomic environments act as plasticity carriers in amorphous silicon. *Physical Review B*, 72 (24), article 245205. https://doi.org/10.1103/PhysRevB.72.245205 (In English)

Demkowicz, M. J., Argon, A. S., Farkas, D., Frary, M. (2007) Simulation of plasticity in nanocrystalline silicon. *Philosophical Magazine*, 87 (28), 4253–4271. https://doi.org/10.1080/14786430701358715 (In English)

Dufour, L.-C., Monty, C., Petot-Ervas, G. (eds.). (1989) *Surfaces and interfaces of ceramic materials*. Dordrecht; Boston; London: Kluwer Publ., 820 p. https://www.doi.org/10.1007/978-94-009-1035-5 (In English)

Glezer, A., Pozdnyakov, V. (1995) Structural mechanism of plastic deformation of nanomaterials with amorphous intergranular layers. *Nanostructured Materials*, 6 (5-8), 767–769. https://doi.org/10.1016/0965-9773(95)00171-9 (In English)

Gutkin, M. Yu., Ovid'ko, I. A. (2009) Plastic flow in amorphous covalent solids and nanoceramics with amorphous intergranular layers. *Reviews on Advanced Materials Science*, 21 (2), 139–154. (In English)

Gutkin, M. Yu., Ovid'ko, I. A. (2010a) A composite model of the plastic flow of amorphous covalent materials. *Physics of the Solid State*, 52 (1), 58–64. https://doi.org/10.1134/S1063783410010105 (In English)

Gutkin, M. Yu., Ovid'ko, I. A. (2010b) Plastic flow and fracture of amorphous intercrystalline layers in ceramic nanocomposites. *Physics of the Solid State*, 52 (4), 718–727. https://doi.org/10.1134/S1063783410040086 (In English)

Gutkin, M. Yu., Ovid'ko, I. A., Pande, C. S. (2004) Yield stress of nanocrystalline materials: Role of grain-boundary dislocations, triple junctions and Coble creep. *Philosophical Magazine*, 84 (9), 847–863. https://doi.org/10.1080/14786430310001616063 (In English)

Gutkin, M. Yu., Ovid'ko, I. A., Skiba, N. V. (2004) Emission of partial dislocations by grain boundaries in nanocrystalline metals. *Physics of the Solid State*, 46 (11), 2042–2052. https://doi.org/10.1134/1.1825547 (In English)

Hoffmann, M. J., Petzow, G. (eds.). (1994) *Tailoring of mechanical properties of Si_3N_4 ceramics*. Dordrecht: Springer Publ., 451 p. https://www.doi.org/10.1007/978-94-011-0992-5 (In English)

Hulbert, D. M., Jiang, D., Kuntz, J. D. et al. (2007) A low-temperature high-strain-rate formable nanocrystalline superplastic ceramic. *Scripta Materialia*, 56 (12), 1103–1106. https://doi.org/10.1016/j.scriptamat.2007.02.003 (In English)

Keblinski, P., Phillpot, S. R., Wolf, D. et al. (1996) Thermodynamic criterion for the stability of amorphous intergranular films in covalent materials. *Physical Review Letters*, 77 (14), 2965–2968. https://doi.org/10.1103/PhysRevLett.77.2965 (In English)

Keblinski, P., Phillpot, S. R., Wolf, D., Gleiter, H. (1997) Amorphous structure of grain boundaries and grain junctions in nanocrystalline silicon by molecular-dynamics simulation. *Acta Materialia*, 45 (3), 987–998. https://doi.org/10.1016/S1359-6454(96)00236-4 (In English)

Kleebe, H. J. (1997) Structure and chemistry of interfaces in Si_3N_4 ceramics studied by transmission electron microscopy. *Journal of the Ceramic Society of Japan*, 105 (1222), 453–475. https://doi.org/10.2109/jcersj.105.453 (In English)

Kleebe, H.-J., Cinibulk, M. K., Cannon, R. M., Rüble, M. (1993) Statistical analysis of the intergranular film thickness in silicon nitride ceramics. *Journal of the American Ceramic Society*, 76 (8), 1969–1977. https://doi.org/10.1111/j.1151-2916.1993.tb08319.x (In English)

Kleebe, H. J., Hoffmann, M. J., Ruehle, M. (1992) Influence of secondary phase chemistry on grain boundary film thickness in silicon nitride. *Zeitschrift für Metallkunde*, 83 (8), 610–617. (In English)

Mo, Y. F., Szlufarska, I. (2007) Simultaneous enhancement of toughness, ductility, and strength of nanocrystalline ceramics at high strain-rates. *Applied Physics Letters*, 90 (18), article 181926. https://doi.org/10.1063/1.2736652 (In English)

Ovid'ko, I. A., Sheinerman, A. G. (2009) Enhanced ductility of nanomaterials through optimization of grain boundary sliding and diffusion processes. *Acta Materialia*, 57 (7), 2217–2228. https://doi.org/10.1016/j.actamat.2009.01.030 (In English)

Ovid'ko, I. A., Skiba, N. V., Sheinerman, A. G. (2008) Influence of grain boundary sliding on fracture toughness of nanocrystalline ceramics. *Physics of the Solid State*, 50 (7), 1261–1265. https://doi.org/10.1134/S1063783408070123 (In English)

Pozdnyakov, V. A., Glezer, A. M. (1995) Anomalies of Hall-Petch dependence for nanocrystalline materials. *Technical Physics Letters*, 21 (1), 31–36. (In English)

Romanov, A. E., Vladimirov, V. I. (1992) Disclinations in crystalline solids. In: F. R. N. Nabarro (ed.). *Dislocations in solids. Vol. 9*. Amsterdam; London; New York: North-Holland Publ., pp. 191–402. (In English)

Subramaniam, A., Koch, C. T., Cannon, R. M., Rühle, M. (2006) Intergranular glassy films: An overview. *Materials Science and Engineering A*, 422 (1-2), 3–18. https://doi.org/10.1016/j.msea.2006.01.004 (In English)

Szlufarska, I., Nakano, A., Vashishta, P. (2005) A crossover in the mechanical response of nanocrystalline ceramics. *Science*, 309 (5736), 911–914. https://doi.org/10.1126/science.1114411 (In English)

Tomsia, A. P., Glaeser, A. M. (eds.). (1998) *Ceramic microstructures: Control at the atomic level*. Boston: Springer Publ., 854 p. https://www.doi.org/10.1007/978-1-4615-5393-9 (In English)

Xu, X., Nishimura, T., Hirosaki, N. et al. (2006) Superplastic deformation of nano-sized silicon nitride ceramics. *Acta Materialia*, 54 (1), 255–262. https://doi.org/10.1016/j.actamat.2005.09.005 (In English)

Zhang, Z. L., Sigle, W., Koch, C. T. et al. (2011) Dynamic behavior of nanometer-scale amorphous intergranular film in silicon nitride by *in situ* high-resolution transmission electron microscopy. *Journal of the European Ceramic Society*, 31 (9), 1835–1840. https://doi.org/10.1016/j.jeurceramsoc.2011.03.016 (In English)

Condensed Matter Physics.
Semiconductor Physics

UDC 538.9

https://www.doi.org/10.33910/2687-153X-2021-2-2-61-67

Local structure of amorphous and crystalline $Ge_2Sb_2Te_5$ films

Yu. A. Petrushin[1], A. V. Marchenko[1], P. P. Seregin✉[1]

[1] Herzen State Pedagogical University of Russia, 48 Moika Emb., Saint Petersburg 191186, Russia

Authors

Yuri A. Petrushin, e-mail: uraordie@mail.ru

Alla V. Marchenko, ORCID: 0000-0002-9292-2541, e-mail: al7140@rambler.ru

Pavel P. Seregin, ORCID: 0000-0001-5004-2047, e-mail: ppseregin@mail.ru

For citation: Petrushin, Yu. A., Marchenko, A. V., Seregin, P. P. (2021) Local structure of amorphous and crystalline $Ge_2Sb_2Te_5$ films. *Physics of Complex Systems*, 2 (2), 61–67. https://www.doi.org/10.33910/2687-153X-2021-2-2-61-67

Received 10 February 2021; reviewed 10 March 2021; accepted 10 March 2021.

Abstract. An effective way to examine structural rearrangement in solids is Mössbauer spectroscopy. A key requirement to Mössbauer probes used for these purposes is the possibility of their localization in a certain site of the crystal lattice or in the structural network of the amorphous material. When absorption spectroscopy is used to examine the local structure of crystalline and amorphous $Ge_2Sb_2Te_5$ films, this requirement is satisfied for ^{119}Sn isotope. Tin atoms ^{119}Sn isovalently substitute germanium atoms in the structure of both vitreous and crystalline germanium tellurides. The absorption Mössbauer spectroscopy on ^{119}Sn impurity centers shows that germanium atoms in the structure of amorphous and polycrystalline $Ge_2Sb_2Te_5$ films have different local symmetries (tetrahedral in the amorphous phase and octahedral in the crystalline).

Keywords: Mössbauer spectroscopy, phase-memory, $Ge_2Sb_2Te_5$, local structure, X-ray fluorescence analysis.

Introduction

Phase-memory (PM) devices based on chalcogenide semiconductors are mostly used at present for reversible transitions from the amorphous to the crystalline state of thin Ge—Sb—Te films, with the composition $Ge_2Sb_2Te_5$ attracting most interest. The compound $Ge_2Sb_2Te_5$ cannot be obtained as bulk glass, but the magnetron sputtering of a target can produce amorphous films. The improvement of PM devices and the technology of their production should be based on the results of a study of the crystallization of amorphous $Ge_2Sb_2Te_5$ films. Obtaining information about the local structure of an amorphous film and comparing it with the crystal structure is paramount to such studies. It is impossible to describe the PM mechanism without knowing the structural transformations in reversible phase transitions between the amorphous and crystalline states. For example, a model of a fast reversible transition from the crystalline to the amorphous state was suggested in the early studies of $Ge_2Sb_2Te_5$ films by the XANES method (X-ray absorption near-edge structure) (Kolobov et al. 2004).

The reversible transition from the amorphous state to the cubic crystalline phase is most frequently used in $Ge_2Sb_2Te_5$-based PM devices. However, the operating temperatures of these devices are limited to 120 °C because of the low thermal stability of the amorphous phase. It was suggested in a recent study (Hu et al. 2020) to replace the amorphous-cubic phase transition with a transition from the metastable cubic to stable hexagonal phase in the same films. This replacement provides a combination of high optical contrast, thermal stability, and a small change in density. It also raises the maximum working temperature of optics to 240 °C. The authors of (Hu et al. 2020) attribute the high optical contrast to an increase in the difference in structural disorder on passing from the cubic phase to the hexagonal. This necessitates the analysis of the structure and structural disorder of both crystalline phases of $Ge_2Sb_2Te_5$.

An effective way to examine structural rearrangement in solids is Mossbauer spectroscopy (Bobokhuzhaev et al. 2020). A key requirement to Mössbauer probes used for these purposes is the possibility of their localization in a certain site of the crystal lattice or in the structural network of the amorphous material. When absorption spectroscopy is used to examine the local structure of crystalline and amorphous $Ge_2Sb_2Te_5$ films, this requirement is satisfied for ^{125}Te, ^{121}Sb as well as ^{119}Sn isotopes. ^{125}Te and ^{121}Sb can serve as probes for tellurium and antimony sites, whereas tin atoms ^{119}Sn isovalently substitute germanium atoms in the structure of both vitreous and crystalline germanium tellurides, as was previously shown (Seregina et al. 1977; Micoulaut et al. 2014; Marchenko et al. 2019). Additionally, it is possible to use emission Mössbauer spectroscopy for the ^{119m}Sn isotope with ^{119}Sb and ^{119m}Te parent nuclei. The parent nuclei are introduced into antimony and tellurium sites, respectively. The daughter Mössbauer probe ^{119m}Sn formed according to the decay scheme of ^{119}Sn and ^{119}Te in Fig. 1 can inherit either antimony sites (if the ^{119}Sb isotope is used) or tellurium sites (if the ^{119m}Te isotope is used). This process allows to obtain the models of antisite defects with tin (as an analog of germanium) at antimony or tellurium sites.

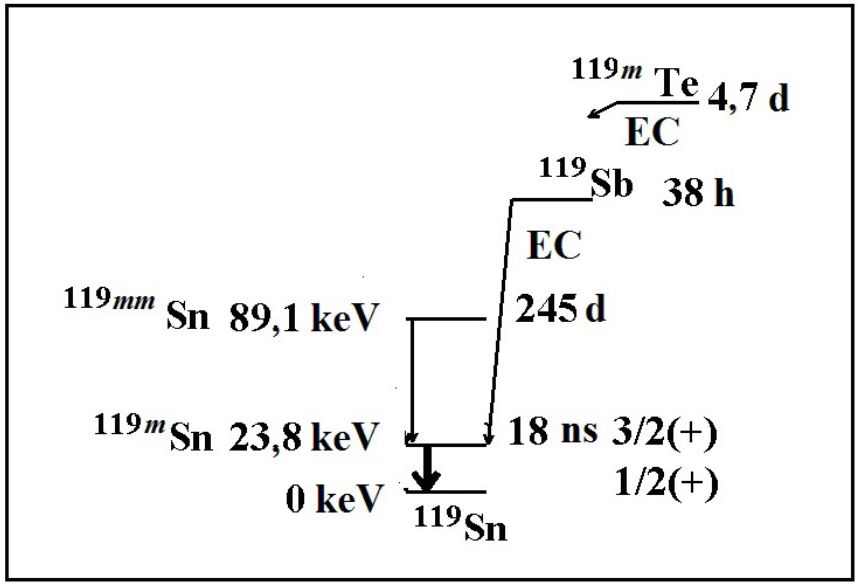

Fig. 1. Scheme of the decay of ^{119mm}Sn, ^{119}Sb, and ^{119m}Te parent isotopes

In this study, we examine the structural rearrangements in $Ge_2Sb_2Te_5$ films by the above-described absorption and emission procedures. The goal of the study is to obtain information about the following:

- structural rearrangements in the local environment of germanium, antimony, and tellurium atoms during the crystallization of amorphous films;
- the nature of tin defects in the structure of crystalline films.

To interpret the obtained results, we also carry out similar studies of the crystalline compounds Sb_2Te_3, GeTe, and vitreous alloy $Ge_{L5}Te_{8.5}$.

Experiment

The compounds under study, $Ge_2Sb_2Te_5$, $Ge_{1.95}Sn_{0.05}Sb_2Te_5$, Sb_2Te_3, and GeTe as well as $Ge_{1.45}Sn_{0.05}Te_{8.5}$, and $Ge_{1.5}Te_{8.5}$ alloys were synthesized from elementary substances at 1050 °C in quartz cells evacuated to 10^{-3} mm Hg.

X-ray-amorphous films of $Ge_2Sb_2Te_5$, $Ge_{1.95}Sn_{0.05}Sb_2Te_5$, $Ge_{1.45}Sn_{0.05}Te_{8.5}$, and $Ge_{1.5}Te_{8.5}$ were produced by dc magnetron sputtering of the target of the corresponding compositions in an atmosphere of nitrogen. The $Ge_{1.95}Sn_{0.05}Sb_2Te_5$ and $Ge_{1.45}Sn_{0.05}Te_{8.5}$ were deposited by using a ^{119}Sn preparation enriched to 92%. Amorphous $Ge_2Sb_2Te_5$ and $Ge_{1.95}Sn_{0.05}Sb_2Te_5$ films were crystallized at 150 °C (to give a cubic *fcc* (face-centered cubic) phase) or at 310 °C (to give a hexagonal *hcp* (hexagonal cubic) phase) (Kato, Tanaka 2005; Shelby, Raoux 2009; Siegrist et al. 2011; Sousa 2011). The amorphous $Ge_{1.5}Te_{8.5}$ and $Ge_{1.45}Sn_{0.05}Te_{8.5}$ films were crystallized at 250 °C.

 https://www.doi.org/10.33910/2687-153X-2021-2-2-61-67

Mössbauer ^{119m}Sn sources based on $Ge_2Sb_2Te_5$ crystalline films (*hcp* phase) were prepared via the diffusion of carrierless ^{119}Sb or ^{119m}Te isotopes into thin amorphous films at a temperature of 310 °C for 10 h. ^{119m}Sn Mössbauer sources based on Sb_2Te_3 and GeTe were prepared via fusion of the corresponding compound with carrierless ^{119}Sb or ^{119}Te in sealed cells.

The ^{119}Sb and ^{119}Te isotopes were produced, respectively, by the reactions ^{119}Sn(*p, n*)^{119}Sb and ^{117}Sn(α, 2*n*)^{119m}Te, with the subsequent chromatographic isolation of carrierless preparations ^{119}Sb and ^{119}Te.

The emission spectra were measured with $CaSnO_3$ as an absorber (surface density in terms of tin 5 mg/cm^2). The spectrum of this absorber with a source of the same composition was a single line with a full width at the half-height G = 0.79(1) mm/s, which was taken to be the instrumental width of the spectral line. For the sources prepared with ^{119m}Te, the spectra were measured after dynamic radioactive equilibrium between the ^{119}Sb and ^{119m}Te isotopes was attained. The isomer shift of the Mössbauer spectra of ^{119m}Sn and ^{119}Sn is presented relative to the $CaSnO_3$ absorber. All the Mössbauer spectra were measured with a CM 4201 TerLab spectrometer at 80 K.

The compositions of the amorphous and crystalline films as well as of the target were monitored by the X-ray fluorescence analysis.

Experimental results and their discussion

Data of the absorption Mössbauer spectroscopy on ^{119}Sn

The typical spectra of ^{119}Sn impurity atoms in amorphous (vitreous) and polycrystalline materials, shown in Figs. 2 and 3, are single broadened lines (G ~ 1.15–1.35 mm/s).

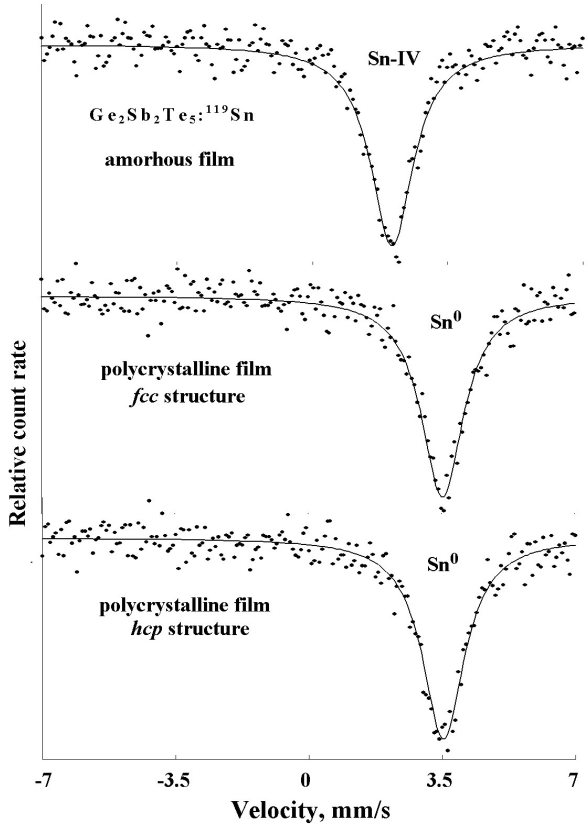

Fig. 2. Absorption Mossbauer spectra of Sn impurity atoms in amorphous and polycrystalline $Ge_2Sb_2Te_5$ films. The positions of spectral lines associated with Sn-IV and Sn^0 centers

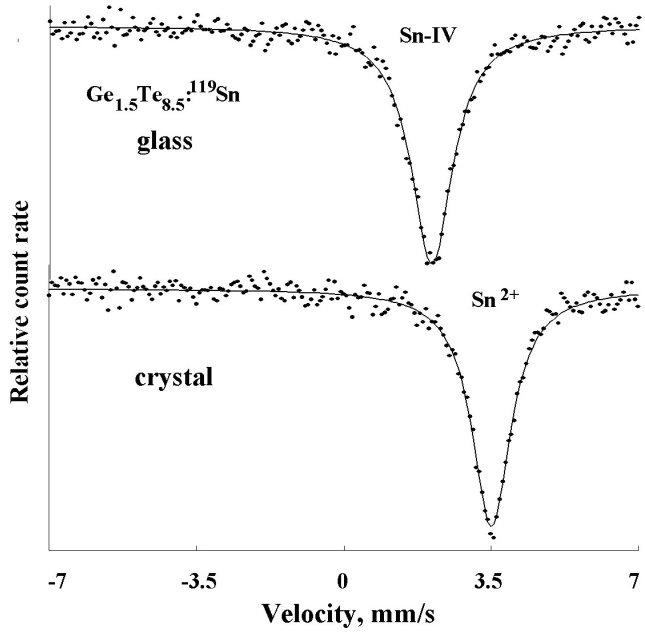

Fig. 3. Absorption Mössbauer spectra of ^{119}Sn impurity atoms in the vitreous and polycrystalline $Ge_{1.5}Te_{8.5}$ alloy. The positions of spectral lines associated with Sn-IV and Sn centers

The spectra of ^{119}Sn for amorphous $Ge_2Sb_2Te_5$ and vitreous $Ge_{x\,5}Te_{85}$ show isomer shifts IS ~ 2.06–2.09 mm/s. These isomer shifts are typical of the spectra of ^{119}Sn compounds of tetravalent tin with a tetrahedral system of Sn-IV chemical bonds (Bobokhuzhaev et al. 2020; Seregina et al. 1977). The ^{119}Sn spectra of the polycrystalline $Ge_2Sb_2Te_5$ samples in both phases, *fcc* and *hcp*, and of $Ge_{15}Te_{85}$ show isomer shifts IS ~ 3.49–3.52 mm/s, which are close to the isomer shift of the ^{119}Sn compound of divalent tin with tellurium, IS = 3.55(2) mm/s, which has the octahedral system of chemical bonds.

The values of the isomer shift of the ^{119}Sn spectra suggest that tin atoms and germanium atoms replaced by tin atoms in the structural network of amorphous $Ge_2Sb_2Te_5$ and vitreous $Ge_{1.5}Te_{8.5}$ form a tetrahedral sp^3 system of chemical bonds. Because germanium (tin) atoms can have only tellurium atoms in their local environment in the structural network of the vitreous alloy, the close values of the isomer shift for all the amorphous materials under study indicate that germanium (tin) atoms are bonded only to tellurium atoms in the structural network of amorphous $Ge_2Sb_2Te_5$. The broadening of the ^{119}Sn spectra of all the amorphous materials under study is due to the lack of long-range order in the position of atoms in these materials—a characteristic property of the Mossbauer spectra of disordered structures.

The fact that the isomer shifts in the ^{119}Sn spectra of polycrystalline $Ge_2Sb_2Te_5$ and $Ge_{1\#5}Te_{8\#5}$ are close to those for the SnTe compound indicates that only tellurium atoms remain upon crystallization in the local environment of germanium (tin) atoms. The widths of the spectra of the polycrystalline samples substantially exceed the instrumental width. This indicates that tin does not form the SnTe compound (crystal lattice of NaCl type) in their composition, but enters into the composition of $Ge_{x-x}Sn_xTe$ solid solutions (in the $Ge_{1.5}Te_{8.5}$ alloy) or into the *fcc* or *hcp* phases (in $Ge_2Sb_2Te_5$ films). According to the X-ray diffraction data, the $Ge_{x-x}Sn_xTe$ solid solutions and the fee $Ge_2Sb_2Te_5$ phase have rhombohedrally distorted lattices of the NaCl type, and the hep $Ge_2Sb_2Te_5$ phase has a lattice with the 9-layered trigonal packing of atoms —Te—Sb—Te—Ge—Te—Te—Ge—Te—Sb— (Kato, Tanaka 2005; Shelby, Raoux 2009; Siegrist et al. 2011; Sousa 2011). Noncubic distortion of the lattices must lead to a quadrupole splitting of the Mossbauer spectra of ^{119}Sn by an amount that is smaller in the given case than the spectral line width.

Data of the emission Mossbauer spectroscopy on ^{119}Sn

In the process of the diffusion doping of $Ge_2Sb_2Te_5$ amorphous films with ^{119}Sb and ^{119m}Te impurity atoms at a temperature of ~300 °C, the films crystallize to give the *hcp* phase (Kato, Tanaka 2005; Shelby, Raoux 2009; Siegrist et al. 2011; Sousa 2011). The typical spectra of ^{119m}Sn impurity atoms formed

 https://www.doi.org/10.33910/2687-153X-2021-2-2-61-67

after the radioactive decay of ^{119}Sb atoms at antimony sites and ^{119m}Te at tellurium sites of the crystal lattice are presented in Fig. 4.

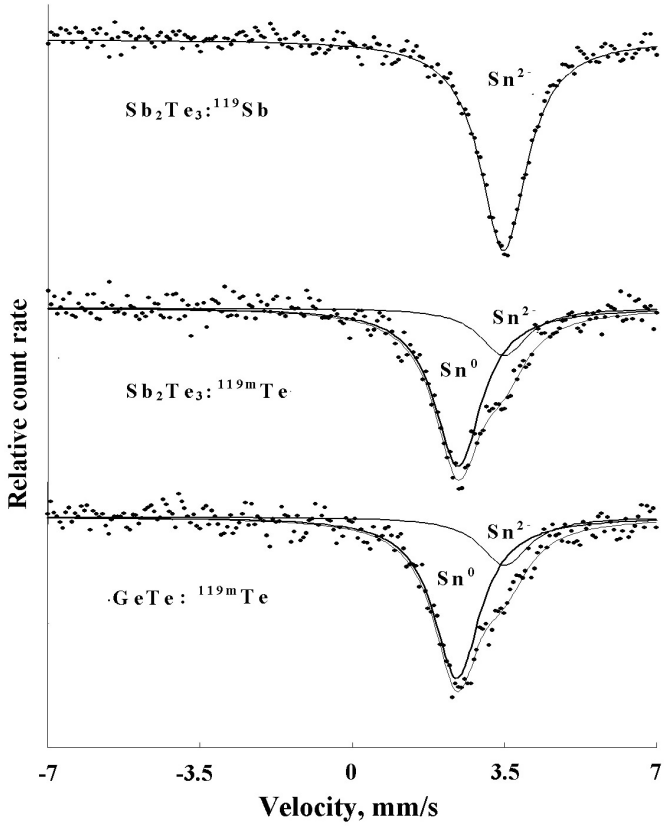

Fig. 4. Emission Mössbauer spectra of ^{119m}Sn impurity atoms formed after the radioactive decay of ^{119}Sb at antimony sites and ^{119m}Te at tellurium sites of a crystalline (*hcp* -phase) $Ge_2Sb_2Te_5$ film. The positions of spectral lines associated with Sn^{2+} and Sn^0 centers

In the case of ^{119}Sb parent atoms, the spectrum has the form of a single broadened line (G = 1.32(2) mm/s). The isomer shift of this spectrum (IS = 3.47(2) mm/s) corresponds to divalent tin Sn^{2+}. The spectrum of ^{119m}Sn impurity atoms formed upon the radioactive decay of ^{119}Sb parent atoms at antimony sites of the crystal lattice of Sb_2Te_3 has similar parameters. Hence follows the conclusion that, in both cases, tellurium atoms are in the local environment of $^{119m}Sn^{2+}$ atoms. This agrees with the data for the *hcp* structure of $Ge_2Sb_2Te_5$ crystalline films (Kato, Tanaka 2005), according to which tellurium atoms are in the local environment of antimony atoms. A conclusion can also be made that there are only tellurium atoms in the local environment of $^{119m}Sn^{2+}$ in both cases.

In the case of ^{119m}Te atoms, the spectrum is a superposition of two broadened lines (G = 1.41–1.46 mm/s). The higher intensity line with the isomer shift IS = 2.42(2) mm/s falling within the range of isomer shifts of the spectra of intermetallic compounds of tin corresponds to $^{119m}Sn^0$ centers formed after the decay of ^{119m}Te mother atoms at tellurium sites. The layered lattice of the hep phase of $Ge_2Sb_2Te_5$ has three types of tellurium layers (Micoulaut et al. 2014), which gives rise to an inhomogeneous isomer shift in addition to a quadrupole splitting and significant broadening of the spectral line.

The weak intensity line with IS = 3.51(2) mm/s is associated with $^{119m}Sn^{2+}$ centers formed after the decay of ^{119m}Te mother atoms shifted from tellurium sites to Sb or Ge sites due to the recoil energy accompanying the radioactive decay of the ^{119m}Te isotope. The set of sites to which the daughter atom of ^{119}Sb is shifted also leads to an inhomogeneous isomer shift and substantial broadening of the spectral line.

A similar structure is observed for the spectra of ^{119m}Sn impurity atoms formed after the radioactive decay of ^{119m}Te atoms at tellurium sites of the crystal lattices of Sb_2Te_3 and GeTe (see Fig. 5), and a conclusion can be made that only tellurium atoms are in all cases in the local environment of $^{119m}Sn^{2+}$ atoms.

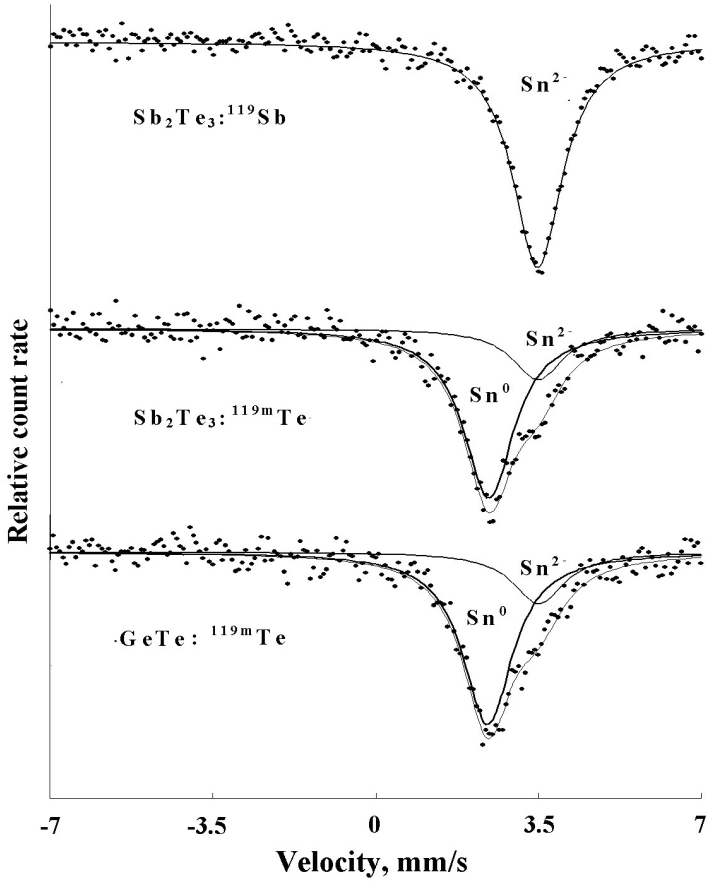

Fig. 5. Emission Mössbauer spectra of ^{119m}Sn impurity atoms formed after the radioactive decay of ^{119}Sb at antimony sites and ^{119m}Te at tellurium sites of the Sb_2Te_3 and GeTe compounds. The positions of spectral lines associated with Sn^{2+} and Sn^0 centers

The ^{119m}Sn atoms that are fixed, due to electron capture from ^{119}Sb or to a chain of electron-capture events from ^{119m}Te, at Sb or Te sites of the hep lattice of $Ge_2Sb_2Te_5$ can be regarded as models of antisite defects because an electronic analog of an atom from one sublattice (germanium) is found at the site of the other sublattice.

Conclusions

It was shown that tin atoms and germanium atoms substituting the former in the structure of amorphous and polycrystalline $Ge_2Sb_2Te_5$ and $Ge_{1.5}Te_{8.5}$ have different local environment symmetries (tetrahedral in the amorphous phase and octahedral in the crystalline phase). The method of emission Mössbauer spectroscopy on ^{119m}Sn impurity centers formed after the radioactive decay of ^{119}Sb and ^{119m}Te mother atoms was used to identify antisite tin defects at antimony and tellurium sites of $Ge_2Sb_2Te_5$ crystalline films. The broadening of the spectra of the antisite defects is accounted for either by a set of possible atoms (antimony, germanium, tellurium) in the local environment of tellurium sites, or by a similar set of sites to which the daughter ^{119}Sb atom is shifted.

References

Bobokhuzhaev, K., Marchenko, A., Seregin, P. (2020) *Structural and antistructural defects in chalcogenide semiconductors. Mossbauer spectroscopy.* S. l.: LAP Lambert Academic Publ., 282 p. (In English)

Hu, C., Yang, Z., Bi, C. et al. (2020) "All-crystalline" phase transition in nonmetal doped germanium–antimony–tellurium films for high-temperature non-volatile photonic applications. *Acta Materialia*, 188, 121–130. https://doi.org/10.1016/j.actamat.2020.02.005 (In English)

Kato, T., Tanaka, K. (2005) Electronic properties of amorphous and crystalline $Ge_2Sb_2Te_5$ films. *Japanese Journal of Applied Physics. Part 1: Regular Papers and Short Notes and Review Papers*, 44 (10R), 7340–7344. https://doi.org/10.1143/JJAP.44.7340 (In English)

Kolobov, A. V., Fons, P., Frenkel, A. I. et al. (2004) Understanding the phase-change mechanism of rewritable optical media. *Nature Materials*, 3 (10), 703–708. https://doi.org/10.1038/nmat1215 (In English)

Marchenko, A. V., Seregin, P. P., Terukov, E. I., Shakhovich, K. B. (2019) Antisite defects in Ge–Te and Ge–As–Te semiconductor glasses. *Semiconductors*, 53 (5), 711–716. https://doi.org/10.1134/S1063782619050166 (In English)

Micoulaut, M., Gunasekera, K., Ravindren, S., Boolchand, P. (2014) Quantitative measure of tetrahedral-sp^3 geometries in amorphous phase-change alloys. *Physical Review B*, 90 (9), article 094207. https://doi.org/10.1103/PhysRevB.90.094207 (In English)

Seregina, L. N., Nasredinov, F. S., Melekh, B. T. et al. (1977) Issledovanie lokal'noj struktury stekol v sistemakh kremnij-tellur, germanij-tellur i germanij-tellur-mysh'yak s pomoshch'yu messbauerovskoj spektroskopii na primesnykh atomakh olova [Study of the local structure of glasses in silicon-tellurium, germanium-tellurium and germanium-tellurium-arsenic systems using Mössbauer spectroscopy on impurity tin atoms]. *Fizika i khimiya stekla — Glass Physics and Chemistry*, 3 (4), 328–331. (In Russian)

Shelby, R. M., Raoux, S. (2009) Crystallization dynamics of nitrogen-doped $Ge_2Sb_2Te_5$. *Journal of Applied Physics*, 105 (10), article 104902. https://doi.org/10.1063/1.3126501 (In English)

Siegrist, T., Jost, P., Volker, H. et al. (2011) Disorder-induced localization in crystalline phase-change materials. *Nature Materials*, 10 (3), 202–208. https://doi.org/10.1038/nmat2934 (In English)

Sousa, V. (2011) Chalcogenide materials and their application to Non-Volatile Memories. *Microelectronic Engineering*, 88 (5), 807–813. https://doi.org/10.1016/j.mee.2010.06.042 (In English)

Condensed Matter Physics. Dielectric Physics

UDC 541.64

https://www.doi.org/10.33910/2687-153X-2021-2-2-68-73

Studying properties of corona electret based on compositions of polylactic acid and bentonite

I. A. Zagidullina[1], R. I. Kamalova[1], M. F. Galikhanov[1], A. A. Guzhova✉[1]

[1] Kazan National Research Technological University, 68 Karl Marx Str., Kazan 420015, Russia

Authors

Inna A. Zagidullina, ORCID: 0000-0002-5736-6957, e-mail: zagidullina_inna@mail.ru

Regina I. Kamalova, e-mail: regikamalova@mail.ru

Mansur F. Galikhanov, ORCID: 0000-0001-5647-1854, e-mail: mgalikhanov@yandex.ru

Alina A. Guzhova, ORCID: 0000-0003-4354-8984, e-mail: alina_guzhova@mail.ru

For citation: Zagidullina, I. A., Kamalova, R. I., Galikhanov, M. F., Guzhova, A. A. (2021) Studying properties of corona electret based on compositions of polylactic acid and bentonite. *Physics of Complex Systems*, 2 (2), 68–73. https://www.doi.org/10.33910/2687-153X-2021-2-2-68-73

Received 19 March 2021; reviewed 29 March 2021; accepted 29 March 2021.

Abstract. The study focuses on the composites of polylactic acid and bentonite as well as corona electrets based on them. The paper explores rheological, electrical, physical and mechanical properties of the composites as well as the effect of corona charging on their properties. Differential scanning calorimetry was used to assess transition temperatures in the compositions. Surface potential, electric field strength and effective surface charge density were measured. Optimal performance was shown by the compositions of polylactic acid with 4% bentonite.

Keywords: polylactic acid, bentonite, corona electret, fine filler, polymer.

Introduction

The global polymer market grows every day. Polymers are used almost in every sphere of our life to produce a wide range of goods for different industries (packaging, electronics, automotive, medicine, agriculture, etc.). However, synthetic polymers have some significant disadvantages—they are made from a non-renewable source (oil) and disposed polymer products are accumulated in landfills causing harmful environmental effects. Environmental concern and industrial policies in many countries that promote natural resource conservation stimulate research, development, production and application of biodegradable polymers. An attractive biopolymer that is now used in the packaging industry is polylactic acid (PLA). It belongs to the group of biodegradable polymers. Its monomer is lactic acid which is produced from renewable plant sources. Polylactic acid undergoes decomposition under both aerobic and anaerobic conditions, while the degradation rate depends on temperature. Properties and processing temperatures of PLA are relatively close to those of bulky polymers (Auras et al. 2010).

One of the fast developing applications of polymers is production of polymer electrets that are used in air filtration, electronic devices, packaging, etc. (Galikhanov et al. 2014; Kestelman et al. 2000; Sessler 1998). In this context production of electret material based on polylactic acid is promising (Galikhanov et al. 2016; Gencheva et al. 2010; Zhang et al. 2020). However, unipolar corona discharge as the fastest and simplest method to obtain an electret is not suitable for polar polylactic acid. In order to change electrical and physical properties of the polymer, attempts were made to introduce fine fillers into the polymer matrix (Gilmutdinova et al. 2017; Guzhova et al. 2016; Ismayilova, Kuliev 2020; Kilic et al. 2013; Kurbanov et al. 2018; Liu et al. 2019).

The objective of the paper was to study electret properties of polylactic acid composites.

Materials and methods

The subject of research was D-polylactic acid (ρ = 1.24 g/cm^3, T_g = 60 °C, T_m = 165 °C) and fine bentonite (d = 0.89 μm, ρ = 0,78 g/cm^3). The polymer and the filler were mixed with Brabender Mixer W 50 EHT. Mixing was performed at temperature of 180 °C for 300 s at blades rotation of 150 rpm. Samples were compression moulded as 0.5 mm films using Gotech GT-7014-H10C according to GOST 12019-66 (Russian standard). Moulding parameters were as follows: temperature—180 °C, pressure—15 MPa, preheating time—5 min, holding-pressure time—5 min, cooling time—5 min.

Charging of the films was done using corona discharge system. It consists of 196 sharp needles uniformly distributed at a square of 49 cm^3. The space between the sample and the charging electrode was 20 mm, polarisation voltage was 30 kV, and polarisation time was 30 s. Before charging, the samples were preheated in a heating chamber at 90 °C for 10 min. The samples were stored in paper envelopes under ambient conditions.

Surface potential V_s, electric field strength E and effective surface charge density σ_{eff} were measured with an IPEP-1 field meter. The measurement error of the electret properties did not exceed 3%. The results given were average values of 5 trials. A differential scanning calorimeter (Q-200TA) was used to assess the effect of the fine filler addition on its transition temperatures. The heating rate was 10 °C/min. The melt flow index was measured according to GOST 11645-73 using an IIRT instrument. The specific volume resistivity ρ_v was measured and calculated according to GOST 6433.2-71. Infrared spectra of the composite materials were obtained with an ATR-FTIR spectrometer InfraLUM FT-08 within the range of 600–4000 cm^{-1}. Stress-strain behaviour of the samples was measured according to GOST 11262-80 using a universal testing machine (Test P 108).

Results and discussion

Polylactic acid is a universal commercial biodegradable thermoplastic material made from lactic acid. It is produced from renewable plant sources such as corn, grains or beetroot.

PLA has insufficient electret properties—low initial surface potential value and fast charge relaxation (Galikhanov et al. 2016; Gencheva et al. 2010; Zhang et al. 2020). Polar groups of the polymer promote trapping of the injected charge carriers by small shallow traps which results in a fast charge decay of the corona electrets. Meanwhile, corona charging has such advantages as high speed, simple apparatus, and uniform charge distribution over the surface.

In order to increase the electret properties of polylactic acid, fine filler was added. Bentonite was used as the filler. It is a hydroalumosilicate, natural swelling clay mineral able to absorb large quantities of water, non-toxic and chemical resistant.

The study of the electret properties of polylactic acid–bentonite compositions revealed the following pattern. An increase in the bentonite content initially improves and then slightly reduces the electret properties of the polymer (Fig. 1); this finding is compliant with the earlier studies (Gilmutdinova et al. 2017; Guzhova et al. 2016; Kilic et al. 2013; Kurbanov et al. 2018).

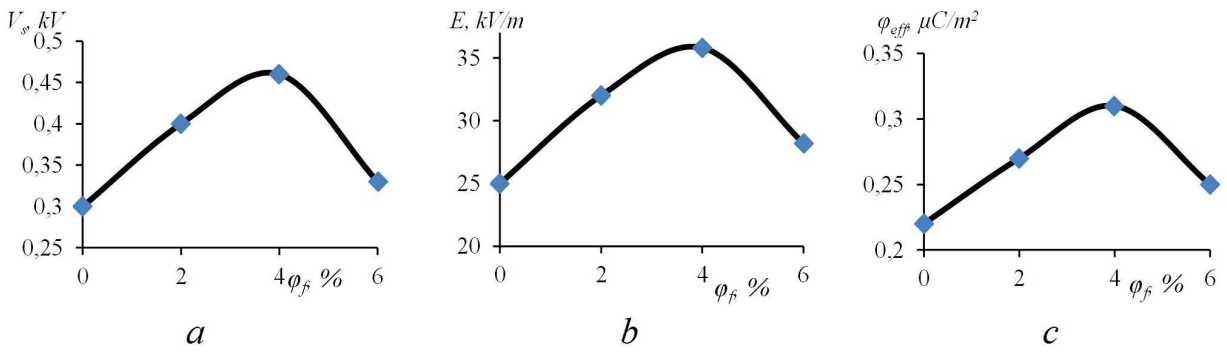

Fig. 1. Surface potential *(a)* electric field strength *(b)* and effective surface charge density *(c)* vs. bentonite content on the 60th day after charging of polylactic acid corona electrets

Fine filler is known to affect the energy depth of the traps of polymers (Galikhanov et al. 2005; Gojayev et al. 2015; Temnov et al. 2013). Besides, filler introduction results in the appearance of new trapping levels (i.e., new categories of traps) of the injected charge carriers. This is the main reason for the electret properties enhancement of the bentonite-filled polylactic acid.

The introduction of fine filler particles into the polymer matrix causes new structural defects that act as charge carrier traps. Filler addition changes size, shape and size distribution of polymer supramolecular structures as well as packing density with filler particles serving as crystal-nucleating agents and a source of crystal imperfection. Besides, adsorption of polylactic acid macromolecules on a solid surface reduces their flexibility that decelerates relaxation processes including the electret state relaxation.

Macromolecule mobility of a polymer can be estimated by both its characteristic temperatures—glass transition or flow temperatures—and rheological properties—melt flow index (MFI).

Fig. 2 illustrates that the position of peaks associated with glass transition (~67–69 °C) and the melting point (~159–162 °C) of polylactic acid filled with 2–6% bentonite changed little, if at all.

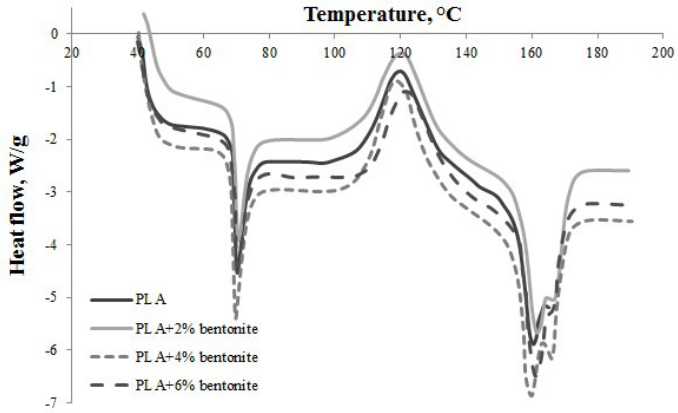

Fig. 2. DSC curves of polylactic acid and its compositions with 2, 4 and 6% bentonite

Many fillers tend to significantly decrease the melt flow index of polymers. The performed study (Table 1) showed that melt flow index decreased, i.e., the viscosity of the melt grew with the increase of the bentonite content.

Table 1. Melt flow index and specific volume resistivity of polylactic acid-bentonite compositions

Sample	*MFI*, g / 10 min	ρv, 10^{12} Ω · *m*
100% PLA	11.2	21
98% PLA + 2% bentonite	10.8	26
96% PLA + 4% bentonite	9.4	29
94% PLA + 6% bentonite	8.9	40

The observed MFI reduction of the polymer can be explained by the fact that solid particles of the filler were not deformed together with the surrounding fluid layers that prevented the fluid flow and increased its viscosity. The flow resistance was increased by macromolecules adsorbed on the filler as well. Besides, collisions of the particles in the flow and energy expenditures on their mutual friction were possible, therefore causing viscosity growth. It is obvious that the higher the bentonite content, the stronger the effect of these factors, and the melt flow index of polylactic acid decreases. Thus, the foregoing assumption that the rate of relaxation processes reduces when polylactic acid is filled with bentonite was proved and it affects the electret properties of compositions.

Another reason for the bentonite effect on the electret properties of polylactic acid can be a change in the electrical resistivity of compositions (Table 1). It is evident that the electrical resistance of PLA compositions slightly grew along with the filler content increase. In other words, the electret properties

 https://www.doi.org/10.33910/2687-153X-2021-2-2-68-73

increase of the filled polylactic acid may occur due to an electrical resistivity change, but to a limited extent (4%), and then other reasons prevail.

Physical and chemical transformations during manufacturing (e.g., mechanical destruction) can significantly affect polymer properties. These transformations are stepped up by the filler. IR spectra of the system under study allow us to estimate chemical structure changes of the bentonite-filled polylactic acid. IR spectroscopy of the samples showed no appreciable difference in the peaks that correspond to oxygen-containing groups of PLA and PLA with bentonite (Fig. 3).

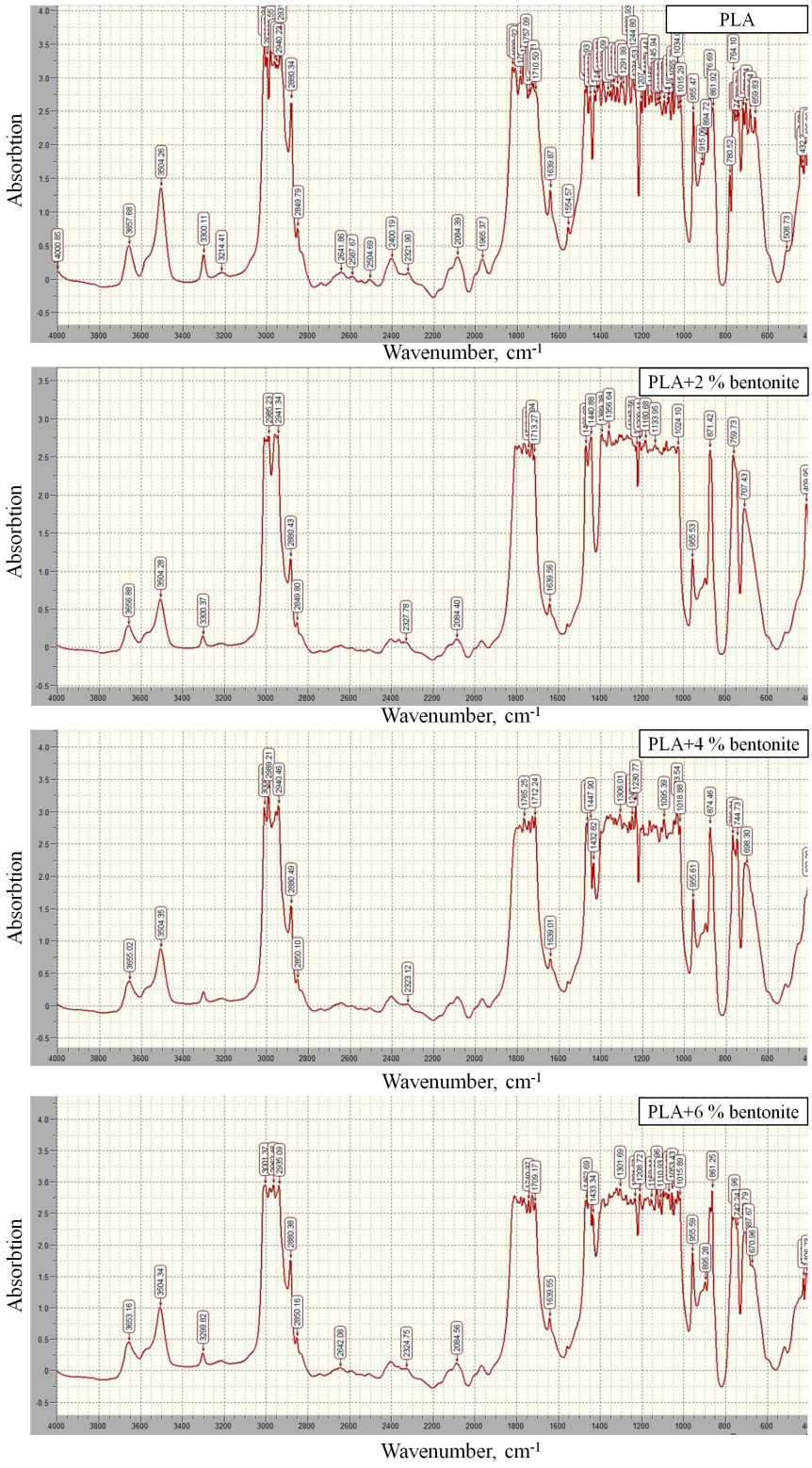

Fig. 3. IR spectra of polylactic acid and its compositions with 2, 4 and 6% bentonite

It implies that the macromolecule oxidation process during the material manufacturing was negligible. Consequently, this reason for the change in the electret properties of polylactic acid when filled with bentonite is not decisive.

With long-term operation of polymer products, the level of their deformation and strength properties comes to the fore. Table 2 shows that with the introduction of bentonite a decrease in the deformation and strength properties of polylactic acid occurs.

Table 2. Stress-strain behaviour of polylactic acid-bentonite compositions

Sample	σ_{UTS}, MPa	ε,%
100% PLA	50.4	8.5
98% PLA + 2% bentonite	40.2	5.3
96% PLA + 4% bentonite	39.7	4.3
94% PLA + 6% bentonite	29.6	3.7

This is due to the fact that bentonite particles are rather big and scarcely deformed with a polymer matrix owing to a great difference in elastic moduli. It results in the formation of overstress and cracks at a polymer-filler interface boundary during the deformation that loosens the composite material.

Conclusion

The obtained results allow us to conclude that the best electret properties were shown by the composition of PLA and 4% bentonite. The increase in the electret properties of the filled polylactic acid was due to the appearance of a new type of injected charge carrier traps at the polymer-filler interface boundary. Changes in the chemical structure, rheological and electrical properties of the filled polymer were of minor importance. The application of polylactic acid and 4% bentonite composition as an electret material that will degrade under environmental conditions after being used can be suggested.

References

Auras, R., Lim, L.-T., Selke, S. E. M., Hideto, T. (eds.). (2010) *Poly(lactic acid): Synthesis, structures, properties, processing, and applications*. Hoboken: John Wiley & Sons Publ., 528 p. https://doi.org/10.1002/9780470649848 (In English)

Galikhanov, M. F., Borisova, A. N., Deberdeev, R. Ya. (2005) Changes in electret characteristics of polymeric formulations in their processing into articles. *Russian Journal of Applied Chemistry*, 78 (5), 820–823. https://doi.org/10.1007/s11167-005-0400-2 (In English)

Galikhanov, M., Guzhova, A., Borisova, A. (2014) Effect of active packaging material on milk quality. *Bulgarian Chemical Communication*, 46 (Special Issue B), 142–145. (In English)

Galikhanov, E., Lounev, I., Guzhova, A. et al. (2016) Study of polylactic acid electret by dielectric spectroscop. *AIP Conference Proceedings*, 1722 (1), article 290002. https://doi.org/10.1063/1.4944288 (In English)

Gencheva, E. A., Yovcheva, T. A., Marudova, M. G. et al. (2010) Formation and investigation of corona charged films from polylactic acid. *AIP Conference Proceedings*, 1203 (1), 495–500. https://doi.org/10.1063/1.3322494 (In English)

Gilmutdinova, A. M., Galikhanov, M. F., Nazarov, N. G. et al. (2017) Increase of value and stability of electret characteristics of polylactide by magnesium oxide modification. *AIP Conference Proceedings*, 1886 (1), article 020092. https://doi.org/10.1063/1.5002989 (In English)

Gojayev, E. M., Ahmadova, K. R., Osmanova, S. S., Aman, S. Z. (2015) Investigation of surface structure and thermostimulated depolarization effect of composite materials with aluminum nano-particles. *American Journal of Nano Research and Applications*, 3 (5), 89–93. (In English)

Guzhova, A. A., Galikhanov, M. F., Gorokhovatsky, Yu. A. et al. (2016) Improvement of polylactic acid electret properties by addition of fine barium titanate. *Journal of Electrostatics*, 79, 1–6. https://doi.org/10.1016/j.elstat.2015.11.002 (In English)

Ismayilova, R. S., Kuliev, M. M. (2020) Features of the charge state of UHMWPE + α-SiO_2 nanocomposites. *Surface Engineering and Applied Electrochemistry*, 56 (3), 267–271. https://doi.org/10.3103/S1068375520030060 (In English)

Kestelman, V. N., Pinchuk, L. S., Goldade, V. A. (2000) *Electrets in engineering: Fundamentals and applications.* Boston: Springer Publ., 281 p. https://doi.org/10.1007/978-1-4615-4455-5 (In English)

Kilic, A., Shim, E., Yeol Yeom, B., Pourdeyhimi, B., (2013) Improving electret properties of PP filaments with barium titanate. *Journal of Electrostatics*, 71 (1), 41–47. https://doi.org/10.1016/j.elstat.2012.11.005 (In English)

Kurbanov, M. A., Ramazanova, I. S., Dadashev, Z. A. et al. (2018) On the electret effect in polymer–ferroelectric piezoceramic composites with various values of the electronegativity of the polymer matrix and piezophase cations. *Semiconductors*, 52 (1), 64–70. http://dx.doi.org/10.1134/S1063782618010128 (In English)

Liu, F., Li, M., Shao, W. et al. (2019) Preparation of a polyurethane electret nanofiber membrane and its air-filtration performance. *Journal of Colloid and Interface Science*, 557, 318–327. https://doi.org/10.1016/j.jcis.2019.08.099 (In English)

Sessler, G. H. (1998) *Electrets. Vol. 1.* Morgan Hill, CA: Laplacian Press, 472 p. (In English)

Temnov, D., Fomicheva, E., Tazenkov, B. et al. (2013) Electrets properties of polyethylene films with starch and aerosil. *Journal of Materials Science and Engineering A*, 3 (7), 494–498. (In English)

Zhang, J., Chen, G., Bhat, G. et al. (2020) Electret characteristics of melt-blown polylactic acid fabrics for air filtration application. *Journal of Appied Polymer Science*, 137 (4), article 48309. https://doi.org/10.1002/app.48309 (In English)

Physics of Semiconductors.
Semiconductor Physics

UDC 536.4+538.9

https://www.doi.org/10.33910/2687-153X-2021-2-2-74-80

Comments on the electronic transport mechanisms in the crystalline state of Ge—Sb—Te phase-change materials

K. Shimakawa✉[1], R. J. Freitas[2]

[1] Gifu University, 1–1 Yanagido, Gifu 501-1193, Japan
[2] National University of Timor Lorosa'e, 10 Rua Formosa, Dili, Timor-Leste

Authors

Koichi Shimakawa, e-mail: koichi@gifu-u.ac.jp

Ruben Jeronimo Freitas, ORCID: 0000-0001-7708-6947, e-mail: ruben.freitas@untl.edu.tl

For citation: Shimakawa, K., Freitas, R. J. (2021) Comments on the electronic transport mechanisms in the crystalline state of Ge–Sb—Te phase-change materials. *Physics of Complex Systems*, 2 (2), 74–80. https://www.doi.org/10.33910/2687-153X-2021-2-2-74-80

Received 14 March 2021; reviewed 1 April 2021; accepted 1 April 2021.

Abstract. It is known that phase-change materials, such as Ge–Sb—Te ternary system, are promising resistive non-volatile random-access memory applications with ultra-rapid reversible transformations between the crystalline and amorphous phases. This class of electronic transition is categorized to be the metal-insulator transition (MIT). The Anderson-type MIT has been discussed extensively in phase-change materials (PCMs) and isothermal annealing of amorphous PCMs (a-PCMs) which, above a certain temperature, leads to the metallic (crystalline) phase. In the insulator regime near the MI transition, Mott-type variable-range hopping (VRH) and/or Efros-Shkolvskii hopping (ESH) at low temperatures below 20 K (and down to 1 K) in $Ge_1Sb_2Te_4$ (GST124) have been discussed extensively, however, we criticize the above argument through a detailed discussion of physical parameters that support the VRH mechanism. It is not clear whether or not the density-of-states (DOS) near the Fermi level is localized (like the Fermi glass) in the crystalline phase. It is also suggested that grain boundaries are expected to interfere with the electronic transport in the crystalline state. We should take into account the grain boundary effects on the electronic transport in the crystalline phase of Ge—Sb—Te system.

Keywords: Ge—Sb—Te phase-change materials, crystalline phase, electronic transport, grain boundary, metal-insulator transition, degenerate semiconductor, dirty metal.

Introduction

In phase-change materials, such as Ge—Sb—Te system, rapid reversible transformations between highly electrically conducting crystalline and resistive amorphous phases are produced by the application of short voltage pulses, realizing random-access memory (called the phase-change random-access memory: PCRAM) (Raoux et al. 2014; Terao et al. 2009; Wuttig, Yamada 2007). The rapid transformations are known to be due to local Joule-heating. On the other hand, it is known that isothermal annealing produces the same type of phase change, which is called the metal-insulator transition (MIT) in GST (Kato, Tanaka 2005; Siegrist et al. 2011; Terao et al. 2009; Volker et al. 2015). One of the examples of the electronic conductivity covering the angular frequency range ω, d. c. – 10^{16} (rad/s), is shown in Fig. 1. Note that the electronic conductivity in the optical frequency range around 10^{15} (rad/s) is often called the *optical conductivity*. We can see a big difference in the electronic conductivity of crystalline (circle) and amorphous (triangle) phases through all frequencies.

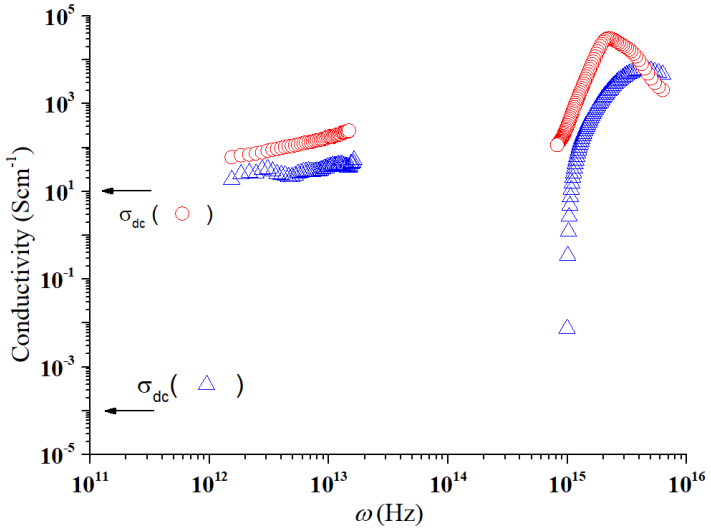

Fig. 1. Frequency dependent conductivity in GST225 films. Open circles and triangles, respectively, are the conductivity in the crystalline phase and the amorphous phase. The arrows indicate the DC conductivity

The Anderson-type MIT (Mott 1993) has been discussed extensively in PCMs (Shimakawa et al. 2013; Siegrist et al. 2011; Volker et al. 2015). Isothermal annealing of amorphous PCMs (a-PCMs) above a certain temperature leads to the metallic (crystalline) phase (Kato, Tanaka 2005; Siegrist et al. 2011; Volker et al. 2015). In the insulator regime near the MIT, Mott-type variable-range hopping (Mott-VRH) (Mott 1993) and/or Efros-Shkolvskii hopping (ESH) (Shklovskii, Efros 1984), at low temperatures below 20 K (and down to 1 K) in $Ge_1Sb_2Te_4$ (GST124), have been discussed in extended (band) states in the crystalline phase (Siegrist et al. 2011; Volker et al. 2015). The disorder-induced localization in the crystalline can be the origin of VRH or ESH near the Fermi level.

In the present report, we criticize the above argument through a detailed discussion of physical parameters that support the VRH or ESH mechanism. It is not clear if the electronic states near the Fermi level are localized in the crystalline phase, such as the Fermi glass. Note also that the effect of grain boundaries is expected to play a significant role in the present system, since the crystalline phase of Ge–Sb—Te nucleated from the amorphous phase has a typical size of 5–20 nm (Siegrist et al. 2011; Wagner et al. 2009).

Metal-insulator transition

The crystalline phase of GST225, for a typical example in Ge—Sb—Te system, is known to have a NaCl type structure with ~20 % of vacancies (Wuttig, Yamada 2007). The deviation from the complete stoichiometry produces degenerate p-type behavior in the crystalline phase (Kim et al. 2007). Annealing of GST225 at 200 °C results in a p-type degenerate crystalline semiconductor with $p \sim 1.5 \times 10^{20}$ cm^{-3}, estimated from the Hall measurement (Siegrist et al. 2011; Volker et al. 2015) and the THz spectroscopy (Shimakawa et al. 2013; Shimakawa et al. 2020) which should show a metallic DC transport behavior; however, note that the conductivity increases with temperature. This is often called the negative temperature coefficient of resistivity (NTCR) and is reported in the so-called "dirty metals" (Mott 1993; Shimakawa et al. 2013). The Fermi level, $E_F = \hbar^2(3\pi p/M)^{2/3}/2m^*$, where M is the valley degeneracy (= 4 for GeSbTe) (Siegrist et al. 2011) and m^* the effective mass which is taken to be $0.3m_e$ (Shimkawa et al. 2013), is deduced to be 0.13 eV. The DOS at the Fermi level in three dimensions (parabolic band), $N(E_F) = 3p/2E_F$, is hence calculated to be 1.7×10^{21} cm^{-3}eV^{-1}.

It is clear that the annealing at above 200 °C produces metallic transport in GST225 and 124 (Shimkawa et al. 2013; Volker et al. 2015). A similar p-value (= 9×10^{19} cm^{-3}) is extracted from the Hall measurement by authors (Volker et al. 2015) (sample "f" in reference), which produces $E_F = 0.10$ eV and $N(E_F) = 1.4 \times 10^{21}$ cm^{-3}eV^{-1} in the crystalline states (after annealing at 175 °C) of GST124. The arguments above strongly suggest that the transport is dominated by free carriers.

The localization may be induced by a structural disorder existing in the crystalline state of the GST system, in particular, near the border of the metal-insulator transition at the annealing temperature

around 150–175 °C. When carriers are strongly localized, the conductivity is expected to be zero (insulator) at low temperatures even if E_F lies in the valence band (Siegrist et al. 2011; Volker et al. 2015). The occurrence of Mott-VRH is therefore suggested at low temperature down to around 1 K (Volker et al. 2015). Note that Mott-VRH is a single-phonon process and the most important factor for Mott-VRH to occur is that the Bohr radius a of localized carriers should be smaller than roughly a half of the optimum hopping distance R_{opt} (Mott, Davis 1979; Mott 1993). If not ($a > R_{opt}/2$), overlapping of localized wave functions occurs and hence the concept of Mott-VRH itself becomes meaningless. Additionally, when $a > a_o$, where a_o is a lattice constant, the localized carriers cannot interact with higher phonon energies leading to a low probability of single-phonon hopping (Mott, Davis 1979; Shimakawa, Miyake 1988).

We should therefore examine whether or not Mott-VRH occurs under the value of $N(E_F)$ stated above, since the $N(E_F)$ is very much higher than the values expected for Mott-VRH in semiconductors or insulators (Volker et al. 2015). In Figures 2 (a), (b) temperature-dependent logarithmic scale of resistivity ρ is plotted against $T^{-1/4}$ and $T^{-1/2}$, respectively, in the crystalline state of GST124. Data are re-plotted for the sample "f" in ref. (Volker et al. 2015). The straight lines in Fig. 2 (a) and (b) indicate the theoretical predictions from Mott-VRH and the ESH, respectively. Note again that Mott-VRH requires that the states near the Fermi level should be localized (uniform density-of-states (DOS) near E_F) and an open-up of the Coulomb gap at the E_F is required in ESH (Shklovskii, Efros 1984) (DOS at E_F is zero).

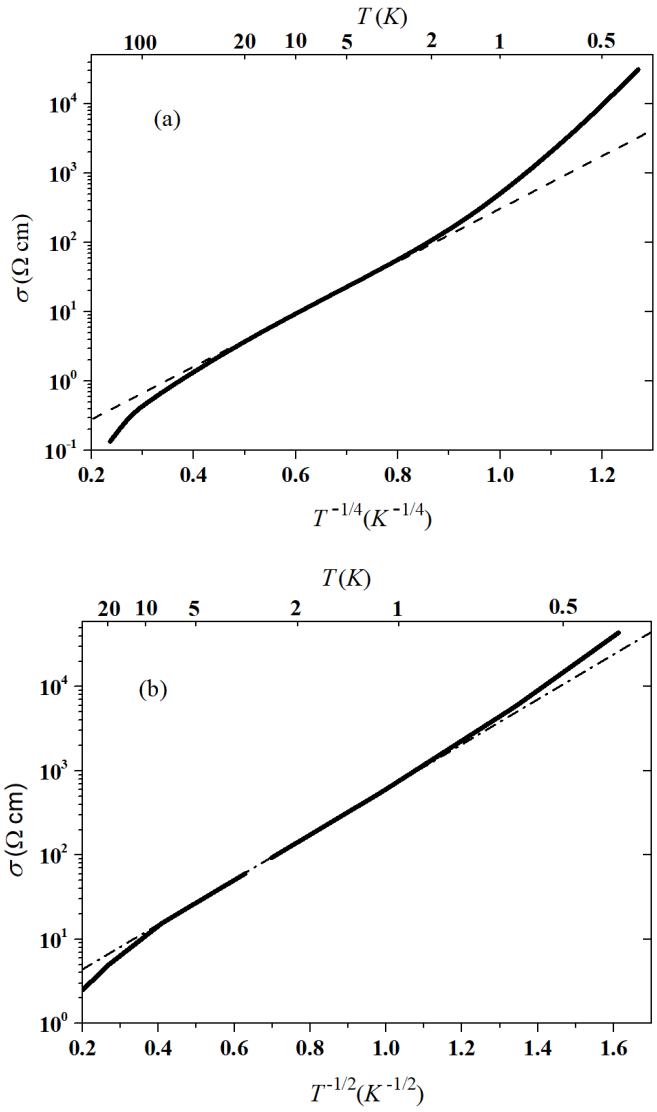

Fig. 2. Temperature dependence of the resistivity in GST124 films; (a) Fitting to the Mott-VRH, (b) Fitting to the Efros-Shklovskii model (Data from (Volker et al. 2015))

https://www.doi.org/10.33910/2687-153X-2021-2-2-74-80

Let us briefly review the Mott-VRH theory as follows. Mott-VRH conductivity is normally given as (Mott, Davis 1979; Mott 1993)

$$\sigma = \sigma_0 \exp\left[-\left(\frac{T_M}{T}\right)^{1/4}\right], \tag{1}$$

with

$$T_M = \frac{\beta}{k_B N(E_F) a^3}, \tag{2}$$

and

$$\sigma_0 = e^2 V_{ph}\left[\frac{N(E_F)a}{32\pi k_B T}\right]^{1/2}, \tag{3}$$

where β is a numerical value around 20, which depends on the details of the model, k_B the Boltzmann constant, a the Bohr radius, and ν_{ph} the phonon frequency which interacts with localized carriers. The hopping length R_{opt} optimizing the hopping rate is given as

$$R_{opt} = \left(\frac{9a}{8\pi N(E_F)kT}\right)^{1/4} = a\left(\frac{9}{8\pi\beta}\right)^{1/4}\left(\frac{T_0}{T}\right)^{1/4}. \tag{4}$$

Volker (Volker et al. 2015) have deduced, by taking β = 18, the following physical parameters in the crystalline state of GST124 (after annealing at 175 °C): T_0 = 5692 K and a = 2.4 nm, and $N(E_F) = 2.5 \times 10^{21}$ cm^{-3}eV^{-1}, from which R_{opt}, for example at 10 K, is estimated to be 1.83 nm. The present values, however, do not support the Mott-VRH, since the necessary condition, $a < R_{opt}/2$, is not satisfied.

From the conductivity prefactor σ_0 (= 19.1 S cm^{-1}) (Volker et al. 2015), using Eq. (3) and taking the same values for a and $N(E_F)$ obtained above, ν_{ph} is estimated to be 5.4×10^{23} s^{-1} which is an unreasonably large value, while Volker deduced a value around 5×10^{11} s^{-1} which looks reasonable but is not a correct value. In the paper by Volker et al. (2015), the presentation of the prefactor (Eq.(10)) is in serious error (their dimension does not give the *conductivity*). It should also be noted that there is the so-called *prefactor problem* in the Mott-VRH theory (Brodsky, Gambino 1972; Ortuno, Pollak 1983; Shimakawa, Miyake 1988), namely, when we use the proper values of a and $N(E_F)$ in Eq. (3), unreasonably large values of ν_{ph} are always produced, and if we use a proper value of ν_{ph}, unreasonably large values of $N(E_F)$ are produced. The estimated value of a (= 2.4 nm) is very much larger than the lattice constant a_0 and hence localized carriers do not interact with high-frequency phonons. It is therefore suggested that a single-phonon process such as Mott-VRH cannot occur under this condition (Mott, Davis 1979; Shimakawa, Miyake 1988).

Let us examine ESH as well in the present material. ESH conductivity is given as (Shklovskii, Efros 1984; Volker et al. 2015)

$$\sigma = \sigma_0' \exp\left[-\left(\frac{T_{ES}}{T}\right)^{1/2}\right], \tag{5}$$

with

$$T_{ES} = 2.8\frac{e^2}{4\pi\varepsilon_0\varepsilon k_B a}, \tag{6}$$

where ε is the static dielectric constant. A good fit to ESH shown in Fig. 2 (b) may indicate that a Coulomb gap at E_F dominates the hopping of localized carriers, and a is extracted to be 13.3 nm (Volker et al. 2015). The same difficulty, however, exists in the ESH theory when we apply ESH to the present material. The most serious problem is the extracted large a which violates the condition

for the single hopping to occur as stated above, while the functional form of ESH fits well to the experimental data. This type of difficulty in ESH has also been pointed out in doped crystalline semiconductors (Zhang et al. 1990).

Now, we should address whether or not the states near E_F (inside the valence band) are localized. A fact that high density of *free* holes ($p > 0.8 \times 10^{20}$ cm^{-3}) in the crystalline state estimated from the Hall effect measurements (at 300 K) indicates that the transport is dominated by free carriers. If, on the other hand, the states are localized, such a large p should not be obtained from the Hall measurements, i.e., hopping of localized carriers does not produce such a large p (Avdonin et al. 2016; Mott 1993; Mott, Davis 1979).

Are the states near E_F actually localized? To answer this question, we will try to give an alternative argument and replot the same resistivity data on the log scale, as shown in Fig. 3. The resistivity appears to decrease linearly with T in the medium temperature range (5–150 K). The behavior is very much similar to the behavior of other well-annealed (> 175 °C) crystalline GST (Shimakawa et al. 2013; Volker et al. 2015) and amorphous metals (Mott 1993), where the temperature-dependent conductivity is dominated by free carriers and empirically given as (Shimakawa et al. 2013)

$$\sigma = \alpha + \beta T^{1/2} + \gamma T, \tag{7}$$

where α, β, and γ are constants (Shimakawa et al. 2013). It is therefore suggested that the valence band is not localized.

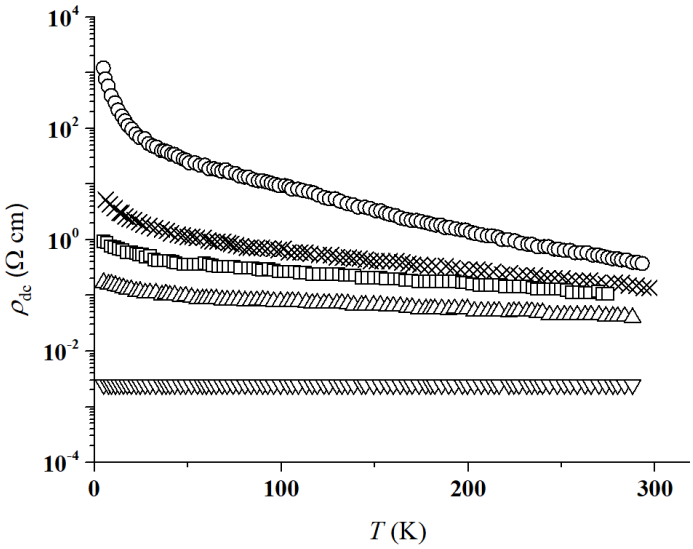

Fig. 3. Temperature dependence of the resistivity ρdc in GST124 films, annealed at 150 °C (◯), 175 °C (×), 200 °C (□), 225 °C (△), 275 °C (▽) (Shimakawa et al. 2013)

The Hall measurements and the THz spectroscopy should be performed at low temperatures to obtain a clear understanding of the low-temperature behavior and of the MIT in GSTs. Unfortunately, there is no report on this issue at low temperatures, and this is something we will discuss in a future paper.

Finally, we briefly discuss the effects of grain boundaries in GST. As we stated earlier, the crystalline phase of Ge—Sb—Te has a typical size of 5–20 nm (Kumar et al. 2013; Siegrist et al. 2011; Wagner et al. 2009), although its size depends on the preparation technique. As shown by open circles at $\omega \approx 10^{13}$ rad/s in Fig. 1, the conductivity does not follow the Drude law ($\propto \omega^{-2}$), which may be attributed to grain boundaries (Shimakawa et al. 2013). High density of localized states may exist at grain boundaries and hence hopping (or tunnelling) transport through the localized state should dominate the electronic transport in low temperatures. This suggests that grain boundaries interfere with the free carrier transport (Shimakawa et al. 2013; 2020). If the grain boundaries dominate the carrier transport in crystalline phase of GST, the above arguments of MIT should be modified to some extent.

 https://www.doi.org/10.33910/2687-153X-2021-2-2-74-80

Conclusions

In the phase-change Ge—Sb—Te ternary system, the electronic transition is categorized to be thermally induced MIT. The Anderson-type MIT has been discussed extensively in this class of PCMs and isothermal annealing of a-PCMs above at a certain temperature leads to the metallic (crystalline) phase. In the insulator regime near the MIT, Mott-VRH and/or ESH at low temperatures below 20 K (and down to 1 K) in GST124 have been discussed extensively, however, we criticized the above argument through a detailed discussion of physical parameters that support the Mott-VRH mechanism. It is not clear whether or not the DOS near the Fermi level is localized (like the Fermi glass) in the crystalline phase. It was also suggested that in some GSTs grain boundaries were expected to interfere with the free carrier transport in the crystalline phase.

Acknowledgements

We would like to thank the CADEFEST 2, Japan International Cooperation Agency (JICA) for the financial support to National University of Timor Lorosa'e.

References

Avdonin, A., Skupiński, P., Grasza, K. (2016) Hall effect in hopping regime. *Physica B: Condensed Matter*, 483, 13–18. https://doi.org/10.1016/j.physb.2015.12.024 (In English)

Brodsky, M. H., Gambino, R. J. (1972) Electrical conduction in evaporated amorphous silicon films. *Journal of Non-Crystalline Solids*, 8–10, 739–744. https://doi.org/10.1016/0022-3093(72)90221-9 (In English)

Kato, T., Tanaka, K. (2005) Electronic properties of amorphous and crystalline $Ge_2Sb_2Te_5$ films. *Japanese Journal of Applied Physics*, 44 (10R), 7340–7344. https://doi.org/10.1143/JJAP.44.7340 (In English)

Kim, J.-J., Kobayashi, K., Ikenaga, E. et al. (2007) Electronic structure of amorphous and crystalline $(GeTe)_{1-x}(Sb_2Te_3)_x$ investigated using hard x-ray photoemission spectroscopy. *Physical Review B*, 76 (11), article 115124. https://doi.org/10.1103/PhysRevB.76.115124 (In English)

Kumar, S., Singh, D., Thangaraj, R. (2013) Structural, electrical and optical study of thermally evaporated $Ge_8Sb_2Te_{11}$ thin films. *Thin Solid Films*, 531, 577–582. https://doi.org/10.1016/j.tsf.2013.01.057 (In English)

Mott, N. F. (1993) *Conduction in non-crystalline materials*. 2nd ed. Oxford: Clarendon Press, 160 p. (In English)

Mott, N. F., Davis, E. A. (1979) *Electronic processes in non-crystalline materials*. 2nd ed. Oxford: Clarendon Press, 608 p. (In English)

Ortuno, M., Pollak, M. (1983) Hopping transport in a-Ge and a-Si. *Philosophical Magazine B*, 47 (6), L93–L98. https://doi.org/10.1080/01418638308228274 (In English)

Raoux, S., Xiong, F., Wuttig, M., Pop, E. (2014) Phase change materials and phase change memory. *MRS Bulletin*, 39 (8), 703–710. https://doi.org/10.1557/mrs.2014.139 (In English)

Shimakawa, K., Miyake, K. (1988) Multiphonon tunnelling conduction of localized π electrons in amorphous carbon films. *Physical Review Letters*, 61 (8), 994–996. https://doi.org/10.1103/PhysRevLett.61.994 (In English)

Shimakawa, K., Kadlec, F., Kadlec, C. et al. (2020) Effects of grain boundaries on THz conductivity in the crystalline states of $Ge_2Sb_2Te_5$ phase-change materials: Correlation with DC loss. *Rapid Research Letter*, 15 (3), article 2000411. https://doi.org/10.1002/pssr.202000411 (In English)

Shimakawa, K., Wagner, T., Frumar, M. et al. (2013) Terahertz and dc current losses and the origin of non-Drude terahertz conductivity in the crystalline states of phase change materials. *Journal of Applied Physics*, 114 (23), article 233105. https://doi.org/10.1063/1.4847395 (In English)

Shklovskii, B. I., Efros, A. L. (1984) *Electrical properties of doped semiconductors*. Berlin: Springer Publ., 388 p. https://doi.org/10.1007/978-3-662-02403-4 (In English)

Siegrist, T., Jost, P., Volker, H. et al. (2011) Disorder-induced localization in crystalline phase-change materials. *Nature Materials*, 10 (3), 202–208. https://doi.org/10.1038/nmat2934 (In English)

Terao, M., Morikawa, T., Ohta, T. (2009) Electrical phase-change memory: Fundamentals and state of the art. *Japanese Journal of Applied Physics*, 48 (8R), article 080001. https://doi.org/10.1143/JJAP.48.080001 (In English)

Volker, H., Jost, P., Wuttig, M. (2015) Low-temperature transport in crystalline $Ge_1Sb_2Te_4$. *Advanced Functional Materials*, 25 (40), 6390–6398. https://doi.org/10.1002/adfm.201500830 (In English)

Wagner, T., Orava, J., Prikryl, J. et al. (2009) Medium-term thermal stability of amorphous $Ge_2Sb_2Te_5$ flash-evaporated thin films with regards to change in structure and optical properties. *Thin Solid Films*, 517 (16), 4694–4697. https://doi.org/10.1016/j.tsf.2009.03.074 (In English)

Wuttig, M., Yamada, N. (2007) Phase-change materials for rewritable data storage. *Nature Materials*, 6 (11), 824–832. https://doi.org/10.1038/nmat2009 (In English)

Zhang, Y., Dai, O., Levy, M., Sarachik, M. P. (1990) Probind the coulomb gap in insulating n-Type CdSe. *Physical Review Letters*, 64 (22), 2687–2689. https://doi.org/10.1103/PhysRevLett.64.2687 (In English)

Theoretical Physics.
General Relativity and Gravity

UDC 524.834

https://www.doi.org/10.33910/2687-153X-2021-2-2-81-86

The forces and Penrose process in Friedman spacetime

A. A. Grib✉[1], V. D. Vertogradov[1, 2]

[1] Herzen State Pedagogical University of Russia, 48 Moika Emb., Saint Petersburg 191186, Russia
[2] Special Astrophysical Observatory of the Russian Academy of Sciences, St Petersburg branch, 65 Pulkovskoe Rd, Saint Petersburg 196140, Russia

Authors

Andrey A. Grib, ORCID: 0000-0002-6389-991X, e-mail: andrei_grib@mail.ru

Vitalii D. Vertogradov, ORCID: 0000-0002-5096-7696, e-mail: vdvertogradov@gmail.com

For citation: Grib, A. A., Vertogradov, V. D. (2021) The forces and Penrose process in Friedman spacetime. *Physics of Complex Systems*, 2 (2), 81–86. https://www.doi.org/10.33910/2687-153X-2021-2-2-81-86

Received 6 March 2021; reviewed 1 April 2021; accepted 1 April 2021.

Abstract. In this paper, we compare the force expressions in both comoving synchronous and Ellis coordinate systems in Friedman-Robertson-Walker spacetime in order to understand how the coordinate transformation affects the inertial forces. We also studied the negative energy problem in Ellis system. The Penrose process is possible outside the apparent horizon due to the fact that the line element has off-diagonal term. However, only the movement towards infinity is possible; we offer the way how one can ascertain that this effect took place outside the apparent horizon.

Keywords: FRW metric, inertial forces, Ellis system, apparent horizon, geodesics, negative energy, Penrose process.

Introduction

In order to describe gravitational force in General Relativity one must study the equations of geodesic lines (Chandrasekhar 1998; Landau, Lifshitz 1980; Weinberg 1972) in the given metric described by some known metric tensor. For example, the leading geodesic equation term in Schwarzschild metric is the Newton force of attraction (Vladimirov 2009). But which are the relevant forces in cosmology as described in the standard Friedman model of the expanding Universe? To answer this question one must write the equations for geodesic lines in Friedmann metric and look for some interpretation of the Christoffel symbols in terms of forces. The form of these symbols is, however, different form in different coordinate systems (Hartle 2002). This occurs because the Christoffel symbols don't obey the tensor law of transformation, which leads to the so called inertial forces being different in different frames. Here, we consider two frames: the comoving synchronous frame and what can be called the Ellis frame (Weinberg 2008). Both frames are widely used in cosmology. The second frame has a more physical appearance, because at small distances it leads to Minkowsky spacetime and only reflects the expansion of the Universe at large distances.This corresponds to the fact that we being on the Earth and in Solar system are not expanding in spite of the fact that on large distances galaxies are expanding. Nevertheless, a synchronous system is well-suited to describe properties of galaxies. In the papers by A. A. Grib and Yu. V. Pavlov (Grib, Pavlov 2021) the radial geodesic movement was studied for these two frames. Here, we shall study the geodesics for angles when the value of the angular momentum is conserved. The structudre of the paper is as folows: first we study the geodesic in the synchronous system, then in the Ellis system and discuss the difference of forces in these two systems.

In the Ellis frame, the metric has the off-diagonal term so one might expect the particles with negative energy to exist outside the apparent horizon. However, the radial movement is only possible towards infinity and there is a question how one can ascertain that the Penrose process occurs outside

the apparent horizon. Here, we offer a method that makes it possible to ascertain whether or not this particle possesed negative energy outside the apparent horizon by estimating the positive energy in comoving frame.

We will write some formulas with m and c to emphasize dimensions but in most of formulas, for simplicity, $G = c = 1$ system of units will be used.

The forces in FRW metric

The Friedman-Robertson-Walker (FRW) metric in the coordinates $\{t, r, \theta, \phi\}$ has the following form:

$$ds^2 = c^2 dt^2 - a^2(t)\left[\frac{dr^2}{1-kr^2} - r^2 d\Omega^2\right]. \tag{1}$$

Here a(t) is the scale factor, k = 0, ±1 corresponds the flat, closed and open Friedman model respectively and $d\Omega^2$ is given by:

$$d\Omega^2 = d\theta^2 + sin^2\theta d\phi^2. \tag{2}$$

It is useful to rewrite the metric (1) in the coordinates $\{t, \chi, \theta, \phi\}$. For this purpose let us make the following transformation:

$$r = f(\chi), \tag{3}$$

where

$$\begin{aligned} &f(\chi) = sin\chi, \text{ for } k = 1, \\ &f(\chi) = \chi, \text{ for } k = 0, \\ &f(\chi) = sinh\chi, \text{ for } k = -1. \end{aligned} \tag{4}$$

Then one obtains the metric in the new coordinates:

$$ds^2 = c^2 dt^2 - a^2(t)[d\chi^2 + f^2(\chi) d\Omega^2]. \tag{5}$$

The f_χ (and f_d see below) force component has been computed by Yu. Pavlov and A. Grib (Grib, Pavlov 2021). The metric (1) possesses spherical symmetry. It means we can choose any plane and only consider movement in this plane. For simplicity let us pick the equatorial plane, for which $\theta = \frac{\pi}{2}$. It is convenient to express the ϕ force component through the angular momentum L. We can derive the expression for L from the lagrangian L:

$$2\mathcal{L} = mc^2\left(\frac{dt}{d\tau}\right)^2 - ma^2(t)\left[\left(\frac{d\chi}{d\tau}\right)^2 + f^2(\chi)\left(\frac{d\varphi}{d\tau}\right)^2\right], \tag{6}$$

$$\theta = \frac{\pi}{2}, \; d\theta = 0,$$

where m is the mass of particle, τ is proper time.

From now on we will use the system of units $M = c = 1$.

Using (6) we can obtain the angular momentum expression:

$$L = -\frac{d\mathcal{L}}{d\dot{\varphi}} = a^2(t) f^2(\chi)\dot{\varphi}. \tag{7}$$

Differentiating (7) with respect to τ we obtain the ϕ component of acceleration:

$$\frac{d^2\varphi}{d\tau^2} = -\frac{L}{a^4(t) f^4(\chi)}\left(2f'(\chi) f(\chi) a^2(t)\frac{d\chi}{d\tau} + 2a(t)\dot{a}(t) f^2(\chi)\frac{dt}{d\tau}\right), \tag{8}$$

 https://www.doi.org/10.33910/2687-153X-2021-2-2-81-86

here dash and overdot mean the partial derivative with respect to χ and t respectively. From (7) one can see that the angular momentum depends on the ϕ component of four-velocity $\frac{d\varphi}{d\tau}$. Hence the following expression:

$$-2L\frac{H}{a^2 f^2}\frac{dt}{d\tau}, \tag{9}$$

corresponds to the force which acts like the Coriolis force. Here $H=\frac{\dot{a}}{a}$ is the Hubble constant. This force is attractive if $L < 0$ and repulsive if $L > 0$.

But in (8) we have the second term:

$$-2L\frac{f'}{a^2 f^3}\frac{d\chi}{d\tau}, \tag{10}$$

which has the squared dependence on the velocity. This term doesn't correspond to any force due to the fact that when we consider the inertial forces we should take the three covariant derivative instead of the usual one and terms which are proportional to $\frac{du^\alpha}{d\tau}\frac{du^\beta}{d\tau}$ are the part of this three covariant derivative.

Looking into the force (9), one can see that it is in direct ratio to the angular momentum and the Hubble constant and in inverse ratio to f^2.

Now let us find the difference in the ϕ force component in the case of $\{t, D, \theta, \phi\}$. For this purpose let us make the following transformation:

$$D = a(t)\chi\,. \tag{11}$$

Again we restore c and m for a few formulas.

In these coordinates the metric is given by:

$$ds^2=\left(1-\frac{H^2D^2}{c^2}\right)c^2dt^2+2\frac{HD}{c}dDdct-dD^2-a^2(t)f^2\left(\frac{D}{a}\right)d\Omega^2\,. \tag{12}$$

In these coordinates we have off-diagonal term $2\frac{HD}{c}dDdct$. The Hubble constant H is positive so when $1 - H^2 D^2$ is less than zero the line element might be timelike due to this off-diagonal term. The surface $D=\frac{c}{H}$ is called the apparent horizon. The region $D=\frac{1}{H}\le D\le+\infty$ has some common features with a black hole. The only radial movement which is allowed is towards infinity. The movement in this region towards the observer at $D = 0$ is forbidden. We will show this in the section below.

Like we did in the previous case, we will obtain the force expression differentiating the angular momentum expression. Again we put the lagrangian in the metric (12) in the following form:

$$2\mathcal{L}=mc^2\left(1-\frac{H^2D^2}{c^2}\right)\left(\frac{dt}{d\tau}\right)^2+2mc\frac{HD}{c}\frac{dt}{d\tau}\frac{dD}{d\tau}-ma^2(t)f^2\left(\frac{D}{a(t)}\right)\left(\frac{d\varphi}{d\tau}\right)^2, \tag{13}$$

$$\theta=\frac{\pi}{2}\,.$$

And the angular momentum L is given by (again we put $m = c = 1$):

$$L=-\frac{d\mathcal{L}}{d\dot{\varphi}}=a^2(t)f^2\left(\frac{D}{a(t)}\right)\dot{\varphi}\,. \tag{14}$$

Now differentiating with respect to τ one can obtain the geodesic equation:

$$\frac{d^2\varphi}{d\tau^2} = -2\frac{L}{a^4(t)f^4\left(\frac{D}{a(t)}\right)}$$
$$\left(\dot{a}(t)a(t)f^2\left(\frac{D}{a(t)}\right)\frac{dt}{d\tau} + \dot{f}\left(\frac{D}{a(t)}\right)f\left(\frac{D}{a(t)}\right)a^2(t)\frac{dt}{d\tau} + \right. \tag{15}$$
$$\left. f'\left(\frac{D}{a(t)}\right)f\left(\frac{D}{a(t)}\right)a^2(t)\frac{dD}{d\tau}\right).$$

One can note that—in contrast to the previous case—here we have three terms. Two of these have the linear dependence from velocity:

$$-2L\left(\frac{H}{a^2f^2} + \frac{\dot{f}}{a^2f^3}\right)\frac{dt}{d\tau}, \tag{16}$$

and one term has the squared dependence on the velocity:

$$-2L\frac{f'}{a^2f^3}\frac{dD}{d\tau}. \tag{17}$$

One can note that the part of three covariant derivative (17) has the same expression as in the previous case [SF (10)]. The ϕ force component (16), however, merits thorough consideration.

Let us note that:

$$\dot{f}\left(\frac{D}{a(t)}\right) = \frac{df}{d\frac{D}{a}}\frac{-DH}{a(t)}. \tag{18}$$

Substituting this into (16) one can obtain:

$$-2L\frac{H}{a^2f^2}\frac{dt}{d\tau}\left(1+\frac{\frac{df}{d\frac{D}{a}}}{af}\right). \tag{19}$$

Now if we consider the new Hubble constant:

$$\tilde{H} = H\left(1+\frac{\frac{df}{d\frac{D}{a}}}{af}\right), \tag{20}$$

then we can write the well-known force expression (7):

$$f_{cor}^{\varphi} = -2L\frac{\tilde{H}}{a^2f^2}. \tag{21}$$

One should note that $\frac{dt}{d\tau} > 0$ because we have the condition of future movement in time, $\tilde{H} > 0$ so as in the previous case this force component might be both attractive and repulsive depending on the sign of the angular momentum L.

 https://www.doi.org/10.33910/2687-153X-2021-2-2-81-86

So if we change the coordinate system, then the force components also changes. Thus the observer should be careful not to mix up $\tilde{H}$ and H.

The negative energy problem

If the metric expression has off-diagonal term then the spacetime can contain particles with negative energy. The energy expression can be obtained from the lagrangian (13):

$$E' = \frac{d\mathcal{L}}{d\dot{t}} = \left(1 - H^2 D^2\right)\dot{t} + HD\dot{D} \,. \tag{22}$$

One can see that the first term becomes negative outside the apparent horizon. However, the metric (12) might still be timelike due to off-diagonal term *2HDdDdt*. For timelike geodesic we have one condition $g_{ik}\frac{dx^i}{d\tau}\frac{dx^k}{d\tau} = 1$. In particular it means that *2L = 1* but outside the apparent horizon it is possible only if $\frac{dD}{d\tau} > 0$. Otherwise we have spacelike geodesic and the particle on this geodesic has the velocity which is bigger than the speed of light and this situation is unphysical.

So the main question we have to answer is how we can observe these particles with negative energy. This type of particles can only form outside the apparent horizon and all particles then move away from the observer. However the apparent horizon is not static one, i.e. it is dynamic. The observer has the same distance for it. So if the four-velocity $\frac{dD}{d\tau}$ of the observer is bigger then the same component of four-velocity of the particle with negative energy, then after this particle can sometimes be seen by observer. However, inside the apparent horizon this particle can't possess the negative energy because $1 - H^2D^2 > 0$ in this region and the energy which the observer measures is positive. To understand whether or not these particles possessed the negative energy outside the apparent horizon we should compare the energy (22) to the energy from the lagrangian (6). Thus, we need to see how the energy depends upon the coordinate transformation. According to the rule of the vector transformation we have:

$$p_i' = \frac{dx^i}{dx'^k} p_k \,, \tag{23}$$

where $p_i = \frac{d\mathcal{L}}{d\dot{x}^i}$ is the four-momentum vector. This rule gives:

$$E' = E - \chi H p_\chi \,, \tag{24}$$

where

$$\begin{aligned} E &= \frac{dt}{d\tau} \,, \\ p_\chi &= \frac{d\chi}{d\tau} \,. \end{aligned} \tag{25}$$

So if the value of $\chi H \dot{\chi}$ is bigger than E then the particle possessed negative energy outside the apparent horizon. Crucially, we evaluate the term $\chi H \dot{\chi}$ outside the apparent horizon.

Conclusion

In this paper we have considered the FRW spacetime in two coordinate systems $\{t, \chi, \phi, \theta\}$ and $\{t, D, \phi, \theta\}$ in order to find out how forces in this spacetime depend upon coordinate transformation for ϕ-force component. We have found that in $\{t, \chi, \phi, \theta\}$ coordinates we only have one expression for the ϕ force component but in $\{t, D, \phi, \theta\}$ we have 2 expressions. Thus, when measuring the Hubble constant one should realize which one is observed, not to confuse the real H Hubble constant with $\tilde{H}$ one. One should also note that this ϕ force component can be attractive $L < 0$ or repulsive $L > 0$, a fact that is shared by both coordinate frames.

We have also considered the negative energy problem. The Penrose process exists outside the apparent horizon but due to the fact that only movement towards infinity is possible one needs to find a way to observe it. We found that if the velocity of the observer $\left(\frac{dD}{d\tau}\right)_{obs}$ is bigger than the velocity of the particle

with negative energy $\left(\frac{dD}{d\tau}\right)_{nep}$ then this particle can appear inside the apparent horizon possessing positive energy. Then the observer can measure its positive energy and using formula (24) in the comoving synchronous frame they can estimate its value outside the apparent horizon tracing along the geodesic the term χHp_{χ}. Using $D = a(t)\chi$ and the fact that D must be bigger than $\frac{H^2D^2}{c^2}$ the observer can say wether or not this energy was negative outside the apparent horizon.

References

Chandrasekhar, S. (1998) *The mathematical theory of black holes.* New York: Oxford University Press, 646 p. (In English)

Grib, A. A., Pavlov, Yu. V. (2021) Some effects of different coordinate systems in cosmology. *The European Physical Journal Plus*, 136 (3), article 318. https://doi.org/10.1140/epjp/s13360-021-01249-7 (In English).

Hartle, J. B. (2002) *Gravity: An introduction to Einstein's general relativity*. Boston: Addison Wesley Publ., 608 p. (In English)

Landau, L. D., Lifshitz, E. M. (1980) *Course of theoretical physics series. Vol. 2. The classical theory of fields.* 4th ed. Oxford: Butterworth-Heinemann, 444 p. (In English)

Vladimirov, Yu. S. (2009) *Klassicheskaya teoriya gravitatsii [Classical gravity theory].* Moscow: Publishing house "Librokom", 264 p. (In Russian)

Weinberg, S. (2008) *Cosmology*. Oxford: Oxford University Press, 544 p. (In English)

Weinberg, S. (1972) *Gravitation and cosmology: Principles and applications of the general theory of relativity*. New York: John Wiley & Sons Publ., 657 p. (In English)

 https://www.doi.org/10.33910/2687-153X-2021-2-2-81-86

Theoretical Physics.
Atomic and Molecular Physics

UDC 539.186 https://www.doi.org/10.33910/2687-153X-2021-2-2-87-92

Eigenfunctions of continuous spectrum in the problem of the two zero range potentials

A. Z. Devdariani[1], A. V. Dadonova✉[2], I. A. Shevtsova[1]

[1] Saint Petersburg State University, 7/9 Universitetskaya Emb., Saint Petersburg 199034, Russia
[2] Herzen State Pedagogical University of Russia, 48 Moika Emb., Saint Petersburg 191186, Russia

Authors

Alexander Z. Devdariani, ORCID: 0000-0002-0605-6705, e-mail: snbrn2@yandex.ru

Alla V. Dadonova, ORCID: 0000-0003-2505-4067, e-mail: alladadonova@mail.ru

Ianina A. Shevtsova, ORCID: 0000-0003-1562-6375, e-mail: shevtsova_jana@mail.ru

For citation: Devdariani, A. Z., Dadonova, A. V., Shevtsova, I. A. (2021) Eigenfunctions of continuous spectrum in the problem of the two zero range potentials. *Physics of Complex Systems*, 2 (2), 87–92. https://www.doi.org/10.33910/2687-153X-2021-2-2-87-92

Received 16 March 2021; reviewed 31 March 2021; accepted 31 March 2021.

Abstract. The paper deals with the application of the method of eigenfunctions of the S-matrix to the problem of two zero range potentials and continues our study of photodetachment, begun in a previous paper (Devdariani, Dadonova 2018). In the case under consideration the eigenfunctions of specific parity depend on two phases that lead to the explicit expressions for the characteristics of scattering and make it possible to construct the proper sets of wave functions for the problems of scattering and photodetachment. An interesting feature of the problem is that the two phases can coincide, which leads to a resonance in the transmission coefficient.

Keywords: zero range potentials, photodetachment, scattering, wafe function, S-matrix, diatomic molecules.

Introduction

The aim of the present work is to continue the study of the electron photodetachment process in diatomic molecules begun in (Devdariani, Dadonova 2018) modeled by two small radius potentials (ZRP). Another goal is to use the S-matrix eigenfunctions for this problem.

The idea of using small-radius potentials as the model of molecule is not new. For example, in (Lapidus 1970), such a model in a one-dimensional version is used to describe a positive molecular hydrogen ion. In (Devdariani, Dadonova 2015; 2018; Devdariani et al. 2014; 2017), the model is used to describe collisions of hydrogen atoms with a negative hydrogen atomic ion, which is much more realistic than using it to describe H_2^+.

The main difficulty in the description of processes involving states of molecular continua is related to the choice of wave functions of continuous spectrum. As a rule, plane waves are used for these purposes. In contrast, the approach based on the use of the exact wave functions of the model problem was proposed and developed in (Dadonova, Devdariani 2012; 2016).

In this paper, the approach based on the application of the S-matrix eigenfunctions (Demkov, Rudakov 1971) is used to construct the wave functions of the continuous spectrum in the one-dimensional and three-dimensional problem. The force centers are described in the framework of ZRP, so that in terms of physical applications we are talking about the process of photodetachment during the collision $H+H^-$. In this work, atomic units are used.

Basis based on the eigenfunctions of the S-matrix

For simplicity, we consider the scattering problem for a symmetric potential in the one-dimensional case. For each momentum value, two linearly independent functions of the continuous spectrum can be constructed. The behavior of an even function is described by the expressions:

$$\Psi_+ = \sin\left(k\left|x-x_1\right|+\delta_+\right)+\sin\left(k\left|x-x_2\right|+\delta_+\right),$$
$$x_{1.2} = \pm\frac{R}{2}.$$

For a behavior of an odd function we have:

$$\Psi_- = \sin\left(k\left|x-x_1\right|+\delta_-\right)-\sin\left(k\left|x-x_2\right|+\delta_-\right),$$

where

$$\Psi_+\left(-x\right) = \Psi_+\left(x\right) \ and \ \Psi_-\left(-x\right) = -\Psi_-\left(x\right).$$

A remarkable feature of these functions is that they diagonalize the S-matrix for an arbitrary symmetric potential $V\left(-x\right)=V\left(x\right)$ with eigenvalues $\exp\left(2i\delta_\pm\right)$. Of course, the functions allow us to write any function of the continuous spectrum of the problem as a linear combination of functions $\Psi_\pm$. For example, let us express the wave function that describes the scattering of an incident plane wave:

$$\Psi\left(x\to-\infty\right) = e^{ikx}+Re^{-ikx},$$
$$\Psi\left(x\to+\infty\right) = Te^{ikx},$$

where R, T are the reflection and transmission coefficients, respectively. For this case, the following equation is true:

$$\Psi\left(x\right) = \alpha\Psi_+\left(x\right)+\beta\Psi_-\left(x\right).$$

Using the asymptotic form of the functions $\Psi_\pm$ gives us:

$$\alpha = e^{i\delta_+},\ \beta = -e^{i\delta_-},$$
$$T = -ie^{i\left(\delta_++\delta_-\right)}\sin\left(\delta_+-\delta_-\right),$$
$$R = -e^{i\left(\delta_++\delta_-\right)}\cos\left(\delta_+-\delta_-\right).$$

It's important to note the resonant character of the coefficients for the following values:

$$\delta_+-\delta_- = 0,\frac{\pi}{2}.$$

We note that $R=f\left(\pi\right)$, where $f\left(\pi\right)$ is a backscattering amplitude and $T-1=f\left(0\right)$, where $f\left(0\right)$ is a forward scattering amplitude. This will be useful when comparing these expressions to the one-dimensional case with the scattering results in the three-dimensional case. The conservation of the normalization gives the optical theorem for the case under consideration:

$$\left|f\left(0\right)\right|^2+\left|f\left(\pi\right)\right|^2 = -2Ref\left(0\right).$$

The use of eigenfunctions of a certain symmetry is especially convenient when calculating processes associated with dipole transitions involving states of the continuous spectrum. Bremsstrahlung, photodetachment and photorecombination can be mentioned as examples of such processes. Bearing in mind the subsequent application to the processes of photorecombination and photodetachment, we write down the following wave function. The asymptotics of this wave function is a converging wave and an outgoing plane waves along or against the axis. For an outgoing wave we have:

 https://www.doi.org/10.33910/2687-153X-2021-2-2-87-92

$$\alpha = e^{-i\delta_+},\ \beta = e^{-i\delta_-},$$

$$\Psi\left(x \to \infty\right) = e^{ikx} + f^*\left(0\right)e^{ikx},$$

$$\Psi\left(x \to -\infty\right) = e^{ikx} + f^*\left(\pi\right)e^{-ikx}.$$

The transition to the amplitudes of converging waves is associated with complex conjugation of the amplitudes of the diverging waves defined above, which corresponds to the general theory of scattering (Landau, Lifshitz 1974).

A zero range potential

Here, for the sake of completeness, we summarize some established results related to the zero potentials. The problem in one-dimension looks as follows. Details of the following formulae can be found in (Demkov, Ostrovskii 1988). We need to solve a Schrodinger equation (in atomic units):

$$-\frac{1}{2}\frac{d\Psi}{dx} = E\Psi$$

with a bounder condition

$$\frac{1}{\Psi}\frac{d\Psi}{dx}\bigg|_{x=0} = -\alpha_0.$$

In the case of a bound state the solution is

$$\Psi^b\left(x\right) = \sqrt{\alpha_0}exp\left[-\alpha_0\left|x\right|\right],$$

$$E = \frac{\alpha_0^2}{2}.$$

For a continuum state we come to

$$\Psi^c\left(x\right) = \frac{1}{\sqrt{\pi}}sin\left[k\left|x\right| + \delta\right],$$

$$E = \frac{k^2}{2}.$$

Considering that

$$\int_{-\infty}^{+\infty}\Psi\left(k\right)\Psi\left(k'\right)dx = \delta\left(k - k'\right),$$

then

$$ctg\left[\delta\right] = -\frac{\alpha_0}{k}.$$

In the three-dimension case, the problem looks as follows:

$$-\frac{1}{2}\Delta\Psi = E\Psi$$

and a bounder condition

$$\frac{1}{r\Psi}\frac{d}{dr}\left[r\Psi\right]\bigg|_{r\to 0} = -\alpha_0$$

or equivalently

$$\Psi(r \to 0) = \frac{1}{4\pi}\left(\frac{1}{r} - \alpha_0\right)$$

with the solution for the bound state

$$\Psi^b = \frac{1}{\sqrt{4\pi\alpha_0}} \frac{exp\left[-\alpha_0 |\vec{r}|\right]}{|\vec{r}|}$$

for $E = -\alpha_0^2 / 2$ and for a continuum state

$$\Psi^c = \frac{1}{\sqrt{4\pi\alpha_0}} \frac{\sin\left[k|\vec{r}| + \delta\right]}{|\vec{r}|},$$

where

$$ctg\left[\delta\right] = -\frac{\alpha_0}{k}.$$

Two zero range potentials. One-dimensional problem

Now let us suppose that there are two equal zero range potentials placed at $x = \pm R / 2$. Then we seek the solution of the Schrodinger equation

$$\left(-\frac{1}{2}\frac{d^2}{dx^2} - \alpha_0\delta\left(x - \frac{R}{2}\right) - \alpha_0\delta\left(x + \frac{R}{2}\right)\right)\Psi = E\Psi.$$

It is obvious that there are two solutions for the bound states: the symmetric (Ψ_+) and antisymmetric (Ψ_-) one

$$\Psi_\pm^b(x) = C_\pm\left(exp\left[-\alpha_\pm\left|x - \frac{R}{2}\right|\right] \pm exp\left[-\alpha_\pm\left|x + \frac{R}{2}\right|\right]\right),$$

where $C_\pm$ are normalization constants; $\alpha_\pm$ are the solutions of the equations:

$$\alpha_\pm = \alpha_0\left(1 \pm exp\left[-\alpha_\pm R\right]\right),$$

which produce two molecular energy terms:

$$E_\pm = -\frac{\alpha_\pm}{2}$$

with

$$E_+(x = 0) = -2\alpha_0^2 \text{ and } E_-(x = 0) = 0.$$

For the free states the choice of solutions depended on the problem, e.g. scattering, photodetachment and so on. However, having in mind the application to the calculations of dipole moments for bound-continuum transition it is reasonable to choose the functions with defined symmetry $\Psi_\pm$

$$\Psi_\pm^c(x) = sin\left[-k\left|x - \frac{R}{2}\right| + \delta_\pm\right] \pm sin\left[-k\left|x + \frac{R}{2}\right| + \delta_\pm\right]$$

with $E = k^2 / 2$. The phase sifts $\delta_\pm$ can be calculated from

$$ctg\left[\delta_\pm\right] = -\frac{\alpha_0}{k}\frac{1 \pm cos\left[kR\right]}{1 \pm \frac{\alpha_0}{k} sin\left[kR\right]}.$$

 https://www.doi.org/10.33910/2687-153X-2021-2-2-87-92

Two zero range potentials. Three-dimensional problem

Again, we construct symmetrical and antisymmetrical functions for the two zero range potentials at $\vec{r}_{01,02} = \pm R/2$:

$$\Psi^b_{\pm}(\vec{r}) = C_{\pm}\left(\frac{\exp\left[-\alpha_{\pm}\left|\vec{r}-\vec{r}_{01}\right|\right]}{\left|\vec{r}-\vec{r}_{01}\right|} \pm \frac{\exp\left[-\alpha_{\pm}\left|\vec{r}-\vec{r}_{02}\right|\right]}{\left|\vec{r}-\vec{r}_{02}\right|}\right),$$

which satisfy the boundary conditions

$$\Psi\left(\vec{r}\to\vec{r}_{01},\vec{r}_{02}\right) = C_{1,2}\left(\frac{1}{r_{01,02}} - \alpha_0\right).$$

$C_{1,2}$ are constants and

$$\alpha_{\pm} = \alpha_0 \pm \frac{exp\left[-\alpha_{\pm}\right]}{R}, E = -\frac{\alpha_{\pm}^2}{2}.$$

The continuum functions for the problem can be taken in the form

$$\Psi^c_{\pm} = \frac{sin\left[-k\left|\vec{r}-\vec{r}_{01}\right|+\delta_{\pm}\right]}{\left|\vec{r}-\vec{r}_{01}\right|} \pm \frac{sin\left[-k\left|\vec{r}-\vec{r}_{02}\right|+\delta_{\pm}\right]}{\left|\vec{r}-\vec{r}_{02}\right|}$$

with

$$ctg\left[\delta_{\pm}\right] = -\frac{\alpha_0}{k}\frac{1\pm\dfrac{cos\left[kR\right]}{\alpha_o R}}{1\pm\dfrac{sin\left[kR\right]}{kR}},$$

at $R = R_0 = \frac{1}{\alpha_0}$ the energy term the antisymmetric bound state interests the boundary of the continuum. It's interesting to note that if $R = R_0$ then equations for $ctg\left[\delta_{\pm}\right]$ for one- and three-dimensional cases coincide. Based on the two independent solutions $\Psi^b_{\pm}$ one can construct the wave functions for scattering and for detachment.

Conclusion

The use of the S-matrix eigenfunctions made it possible to construct the exact wave functions at all values of the electron coordinates. Since the constructed functions possess a certain symmetry with respect to the inversion, they are convenient for calculating the dipole moments of the transitions for the states of the continuous spectrum. The latter remark is fully valid for the ZRP-based models of multi atomic molecules (Demkov, Rudakov 1971) as well.

References

Dadonova, A. V., Devdariani, A. Z. (2012) H^- – H Collision induced radiative transitions. *Journal of Physics: Conference Series*, 397, article 012040. https://doi.org/10.1088/1742-6596/397/1/012040 (In English)

Dadonova, A. V., Devdariani, A. Z. (2016) Radiative transitions in quasimolecules: H^+ H^- collisions. *Journal of Physics: Conference Series*, 769, article 012043. https://doi.org/10.1088/1742-6596/769/1/012043 (In English)

Dadonova, A., Devdariani, A., Dalimier, E., Angelo, P. (2017) Bound-free transitions in H + H^- collisions. *Journal of Physics: Conference Series*, 810, article 012027. https://doi.org/10.1088/1742-6596/810/1/012027 (In English)

Devdariani, A. Z., Dadonova, A. V. (2015) Radiative transitions under H + H^- collisions. *Russian Journal of Physical Chemistry B*, 9 (4), 591–592. https://doi.org/10.1134/S1990793115040181 (In English)

Devdariani, A., Dadonova, A. (2018) Svyazanno-svobodnye perekhody pri stolknoveniyakh H+H^- v odnomernom sluchae [Bound-free electron transitions for one-dimensional H+H^- collisions]. *Universitetskij nauchnyj zhurnal — Humanities & Science University Journal*, 37, 49–54. (In English)

Devdariani, A., Dadonova, A., Shevtsova, J. (2014) Radiative transitions under resonance charge exchange. H + H^- collisions. *Journal of Physics: Conference Series*, 548, article 012018. https://doi.org/10.1088/1742-6596/548/1/012018 (In English)

Demkov, Yu. N., Ostrovskii, V. N. (1988) *Zero-range potentials and their applications in atomic physics.* Boston: Springer Publ., 296 p. https://doi.org/10.1007/978-1-4684-5451-2 (In English)

Demkov, Yu. N., Rudakov, V. S. (1971) The method of partial waves for a nonspherical scatter. *Soviet Physics JETP*, 32 (6), 1103–1109. (In English)

Landau, L. D., Lifshitz, E. M. (1974) *Teoreticheskaya fizika. T. 3. Kvantovaya mekhanika. Nerelyativistskaya teoriya [Theoretical physics. Vol. 3. Quantum mechanics. Non-relativistic theory].* Moscow: Nauka Publ., 768 p. (In Russian)

Lapidus, R. (1970) One-dimensional model of a diatomic ion. *American Journal of Physics*, 38 (7), 905–908. https://doi.org/10.1119/1.1976491 (In English)